nature methods

Article

https://doi.org/10.1038/s41592-023-01845-8

Photoselective sequencing: microscopically guided genomic measurements with subcellular resolution

Received: 11 July 2022

Accepted: 13 March 2023

Published online: 27 April 2023

Check for updates

Sarah M. Mangiameli[1,2], Haiqi Chen[1,3,4], Andrew S. Earl[2], Julie A. Dobkin[1], Daniel Lesman[1], Jason D. Buenrostro[1,2] & Fei Chen[1,2]

In biological systems, spatial organization and function are interconnected. Here we present photoselective sequencing, a new method for genomic and epigenomic profiling within morphologically distinct regions. Starting with an intact biological specimen, photoselective sequencing uses targeted illumination to selectively unblock a photocaged fragment library, restricting the sequencing-based readout to microscopically identified spatial regions. We validate photoselective sequencing by measuring the chromatin accessibility profiles of fluorescently labeled cell types within the mouse brain and comparing with published data. Furthermore, by combining photoselective sequencing with a computational strategy for decomposing bulk accessibility profiles, we find that the oligodendrocyte-lineage-cell population is relatively enriched for oligodendrocyte-progenitor cells in the cortex versus the corpus callosum. Finally, we leverage photoselective sequencing at the subcellular scale to identify features of chromatin that are correlated with positioning at the nuclear periphery. These results collectively demonstrate that photoselective sequencing is a flexible and generalizable platform for exploring the interplay of spatial structures with genomic and epigenomic properties.

The sequence and structure of the genome encodes the information that underlies cell state and function. This structure is organized across diverse length scales. At the subcellular scale, the arrangement of the genome and associated proteins within the volume of the nucleus is a central regulator of gene expression programs[1–4]. This includes transcriptional activation by enhancer–promoter interactions or sequestration of biologically inactive sequences to heterochromatic domains throughout the nucleus[5,6]. Within complex tissues, cells respond to environmental cues or intercellular signaling through diverse transcriptomic and epigenomic states[7–9]. A complete understanding of the interplay between spatial structures and sequence-based information will require new methods that simultaneously measure these properties.

One emerging strategy is to perform a genomic or epigenomic measurement within particular spatial regions under the guidance of microscopic visualization[10–14]. For example, laser-capture microdissection and patch pipette aspiration are early implementations of this strategy where the relevant subpopulation of cells is physically excised from the sample before downstream sequencing-based analysis[15–17]. However, these methods do not have subcellular spatial

---

[1]Gene Regulation Observatory, The Broad Institute of MIT and Harvard, Cambridge, MA, USA. [2]Department of Stem Cell and Regenerative Biology, Harvard University, Cambridge, MA, USA. [3]Cecil H. and Ida Green Center for Reproductive Biology Sciences, University of Texas Southwestern Medical Center, Dallas, TX, USA. [4]Department of Obstetrics and Gynecology, University of Texas Southwestern Medical Center, Dallas, TX, USA. e-mail: jbuen@broadinstitute.org; chenf@broadinstitute.org

resolution, are subject to contamination from neighboring cells and can be laborious if large numbers of individual cells are needed. A similar class of methods use photochemistry to capture nucleic acids from specific regions within a sample[10]. However, the methods largely apply to transcriptomic measurements and are suitable only for analyzing entire nuclei (that is, not mitochondrial or other extranuclear DNA), and most do not provide subcellular resolution.

In this article, to address these shortcomings, we introduce photoselective sequencing (PSS), a new method for sequencing DNA from spatial regions of interest (ROIs) within a fixed biological specimen (Fig. 1a).

Results

The PSS workflow

PSS breaks down into four basic stages: (1) construction of a photocaged DNA-fragment library in situ, (2) selective uncaging of the library using targeted illumination with near-ultraviolet (UV) light, (3) sample digestion and library purification, and (4) amplification of uncaged fragments followed by sequencing on an Illumina platform (Fig. 1a). During the in situ library construction stage, we use Tn5 transposase to produce a library of DNA fragments that are flanked by adapter sequences (tagmentation). Direct transposition of the sample assays chromatin openness (assay for transposase-accessible chromatin using sequencing (ATAC-seq) library; Fig. 1a, step 1)[18]. However, transposase-mediated library preparations have been adapted for both whole-genome and protein-targeted fragmentation in situ[19,20].

To visualize the fragment library and reversibly block amplification, we use customized tagmentation adapters conjugated to a fluorophore using a photocleavable spacer (Fig. 1a, step 1). We next visualize the sample by microscopy and use fluorescent stains to guide ROI identification (Fig. 1a, step 2). Automated in-line image segmentation enables us to scalably assay thousands of individual ROIs localized throughout the sample. Selective illumination of the ROIs using a 405 nm laser line cleaves the fluorophores from the blocked adapters, revealing a 5′ phosphate group. After purification of the library from the sample (Fig. 1a, step 3), indexed secondary adapters containing priming sites for library amplification are ligated only to fragments where the 5′ phosphate groups were previously revealed through photocleavage (Fig. 1a, step 4). Caged fragments do not have available 5′ phosphates and cannot pass the ligation stage (Fig. 1a, step 4, red box). Successfully ligated fragments undergo a gap fill step and are amplified from the secondary adapters to produce sequencing-competent fragments, which are read out an Illumina platform (Extended Data Fig. 1a).

Validating the PSS workflow

To validate the PSS workflow, we first characterized ATAC-seq libraries in adherent cultured cells. To do this, we treated fixed and permeabilized HeLa cells with freely diffusing Tn5 transposase, which preferentially inserts into open chromatin regions[18,21,22]. Library generation was verified by visualization of the fluorescent label on the blocked tagmentation adapters (Fig. 1b, left image). When a subset of nuclei were exposed to near-UV light by scanning a focused 405 nm laser through these regions (Fig. 1b, Extended Data Fig. 1b,c and Supplementary Video 1), we observed an accompanying 97.5% (±1.9% standard deviation (s.d.), $N = 6$ cells) decrease in fluorescence intensity within the exposed nuclei (Fig. 1b (right), Extended Data Fig. 1d,e and 'Intensity decrease during uncaging section' in Supplementary Methods). We next examined the sequencing characteristics of ATAC-seq libraries generated through the PSS workflow. To do this, we uncaged all fragments within the nuclei of 800 individual HeLa cells before digesting the sample and purifying the libraries. We ligated secondary adapters to the unblocked fragments via the free 5′ phosphate group, and subsequently used these adapters as polymerase chain reaction (PCR) handles to generate the final sequencing libraries. After aligning the sequencing reads to the human genome, we observed a periodic fragment size distribution, a hallmark property of ATAC libraries that indicates sensitivity to nucleosome positioning (Fig. 1c, left). Furthermore, we observed a high insertion frequency across transcription start sites (TSSs) genome wide, as indicated by a strong peak in the TSS enrichment plot (Fig. 1c (right) and 'Sequencing alignment and preprocessing' section in Supplementary Methods).

To assess the baseline efficacy of the PSS caging mechanism, we characterized the frequency of fragments in the absence of near-UV light exposure ('Blocking efficiency' section in Supplementary Methods). Briefly, we constructed and purified caged PSS libraries using wells of HeLa cells or mouse brain slices. Once in solution, we split the purified libraries into paired halves, each with equivalent numbers of fragments. We processed and sequenced one member of each pair without uncaging (to measure the number of noise fragments), and the other with complete uncaging (to measure the total number of fragments) (Fig. 1d, schematic). By comparing the library sizes across each pair, we found the caging mechanism to be 99.85% and 99.95% effective cells and tissues, respectively (Fig. 1d, right), demonstrating the robustness of the PSS method.

We next quantified the signal-to-noise ratio (SNR) for PSS experiments. Given the noise mechanism, we expect the number of noise fragments to scale with the total number of nuclei in the sample (and correspondingly the total amount of fragmented DNA), while the number of signal fragments is proportional to the selected sample area. Therefore, we calculated the relationship between the SNR and the fraction of nuclei selected in situ, or equivalently, the fraction of the total nuclear area that is selected (Fig. 1e,f). To do this, we selected various proportions of the nuclei within cultured cells or tissue sections and measured the resulting total number of sequenceable fragments (Supplementary Table 1; $n = 17$ wells, $n = 16$ tissue sections). To estimate the number of noise fragments, we sequenced caged libraries from paired specimens that were protected from near-UV light, but otherwise treated identically to the selected counterparts. We quantified the SNR, where the signal is defined as the total number

Fig. 1 | PSS enables genomic and epigenomic profiling with high spatial resolution. a, Schematic diagram illustrating the PSS method: (1) a library is prepared in situ using a Tn5 transposome (blue) with photocleavable adapters (red and green). The transposase fragments the genome, adding the adapters to each segment (middle). Exposure of the PSS adapter to near-UV light breaks a photocleavable linker, releasing the fluorescent label and revealing a phosphate group (right). (2) Targeted illumination is performed within specific ROIs identified by fluorescence imaging. (3 and 4) The library is purified and adapters are ligated to previously unblocked fragments (yellow and blue), which act as PCR handles for library amplification. gDNA, genomic DNA; ad., adapter. Blocked fragments do not pass the ligation stage (red box). The amplified library is read by next-generation sequencing. **b**, Uncaging an ATAC-seq library (magenta) in HeLa cells. The yellow-outlined nuclei are exposed to near-UV light, cleaving the fluorophore from the adapter (compare before and after image; starred cell shown in zoom) and resulting in a 97.5% (±1.9%, s.d.) intensity decrease (violin plot; $N = 6$ cells, 1 experiment). Nontargeted cells (blue outlines) do not decrease intensity (violin plot; mean 101 ± 1.5% s.d.; 7 cells, 1 experiment). Horizontal lines represent the mean and shaded areas represent the kernel density estimate of the data. Cl., cleaved; Bl., blocked. **c**, Quality metrics for PSS ATAC-seq libraries. Insert size distribution (left) periodicity indicates sensitivity to histone positioning, and pileup plot shows high insertion frequency at TSSs (right). Coverage trace (bottom) shows peaks upstream of highly expressed genes. **d**, Schematic diagram illustrates the procedure for measuring the efficiency of the PSS blocking mechanism. Graph shows blocking efficiency for cells ($N = 13$ wells, 3 experiments) and tissues ($N = 10$ sections, 4 experiments). The mean (line) and raw data (dots) are indicated. On average, >99.95% of fragments are sequencing incompetent without near-UV light exposure. **e**, SNR as a function of the fraction of cultured cells selected ($N = 20$ wells, 3 experiments). Inset shows enlargement of boxed region (red). **f**, SNR as a function of the fraction of cells selected within tissue sections ($N = 16$ sections, 4 experiments).

of fragments in the selected sample minus the inferred number of noise fragments from the caged sample ('Signal-to-noise ratio' section in Supplementary Methods). We note that the range in the fraction of nuclei selected (Fig. 1e,f) is typical for experiments in cells or tissues, and find that the SNR is approximately 5,301 or 5,948 times the fraction of nuclei selected in the respective sample types. Notably, PSS produces high-quality libraries with SNR >16 even if only 0.3% of the sample is selected (Fig. 1f).

PSS reproduces published ATAC-seq data in the mouse brain

To validate and demonstrate the PSS method, we generated chromatin accessibility profiles for both the dentate gyrus region and oligodendrocyte-lineage cells within the mouse brain (Fig. 2a). The dentate gyrus region can be identified through tissue morphology and is composed primarily of hippocampal granule cells.

(Fig. 2b, top image). Conversely, oligodendrocyte-lineage cells, which include mature oligodendrocytes and oligodendrocyte

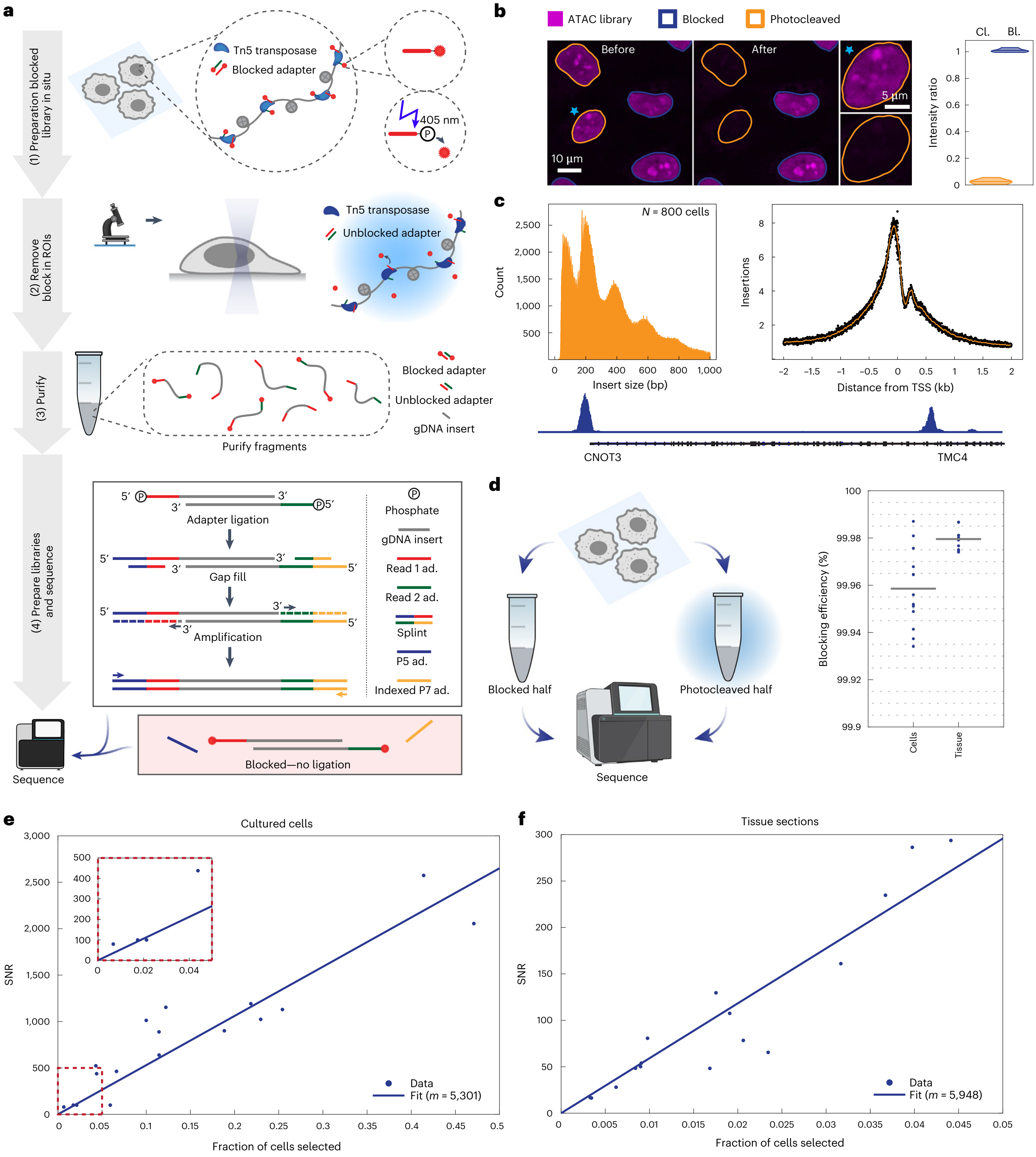

precursor cells (OPCs), are scattered throughout the entire brain and are identifiable via an immunostain against OLIG2 (Fig. 2b, bottom image). We selected these targets to demonstrate photoselection on various morphological traits, and because single-cell ATAC-seq (scATAC-seq) data are readily available for benchmarking the accessibility profiles of the associated cell types[23,24].

To implement PSS for the dentate gyrus and oligodendrocyte-lineage cells, we collected a series of 10 µm tissue sections from a fresh-frozen mouse brain (Extended Data Fig. 2a and Methods). For dentate gyrus selection, sections were acquired from the hippocampal region. To investigate any region-specific differences in oligodendrocyte-lineage cells, sections were collected from both the anterior and posterior brain regions. Tissue sections for oligodendrocyte-lineage cell selection were immunostained for OLIG2, and all sections underwent the in situ phase of the PSS library preparation (Fig. 1a, step 1), and were stained with DRAQ5 (far-red DNA stain) to visualize nuclei. During the photoselection phase (Fig. 1a, step 2), nuclei within the dentate gyrus region were automatically detected on the basis of proximity to neighboring nuclei ($n = 4$ biological replicates, each with approximately 1,800 selected cells; Fig. 2b (yellow outlines) and 'Photoselection' section in Methods). Similarly, oligodendrocyte-lineage cells were detected algorithmically by identifying nuclei with a high fluorescence intensity from the OLIG2 immunofluorescent marker ($n = 6$ biological replicates, each with approximately 1,700 selected cells; Fig. 2b (red outlines) and 'Photoselection' section in Methods). We selectively illuminated the target nuclei with near-UV light and then completed the remainder of the library preparation (Fig. 1a, steps 3–4), including sequencing on an Illumina platform. Preliminary analysis of the sequencing data for all samples showed a strong enrichment of reads in TSSs and a periodic insert size distribution (TSS scores 12–15; Extended Data Fig. 2b–e), and revealed that PSS detects 1,372 reads per selected cell on average (Extended Data Fig. 2f and Supplementary Table 1).

For validation, we verified that the individual PSS replicates were strongly correlated ($r > 0.9$; Extended Data Fig. 2g), and then compared the pooled PSS accessibility profiles with those of aggregated granule cells and oligodendrocytes from an annotated scATAC-seq dataset[23]. Visual comparison of the scATAC-seq and PSS profiles at marker gene loci for the respective cell types suggest a strong agreement between the two approaches (Fig. 2b (traces) and 'Smoothed coverage traces' section in Methods). To quantitatively characterize the correlation between the PSS and scATAC-seq data genome wide, we first performed cisTopic analysis on the scATAC-seq data to generate a reference set of *cis*-regulatory control regions (topics) for further analysis ('cisTopic analysis' section in Methods)[24,25]. We show the clustered scATAC-seq data (based on cisTopic z-score) in the Uniform Manifold Approximation and Projection (UMAP) representation, with the relevant clusters annotated (Fig. 2c). We next leveraged the topics regions to jointly analyze the PSS and scATAC-seq data. To do this, we quantified the cisTopic z-scores for each PSS replicate and the cluster-aggregated scATAC-seq data, calculated the pairwise Pearson correlation coefficients and visualized the results as a hierarchically clustered heat map (Fig. 2d, sections 1–6). The results show a high level of reproducibility between replicate PSS samples, and that the PSS accessibility profiles strongly correlate with those of the corresponding cell types in the single-cell data (Fig. 2d, red-labeled columns 1, 3 and 4 show single-cell reference data).

Notably, the oligodendrocyte-lineage cell accessibility profiles from anterior (bregma ~2.2 mm, cortex and anterior olfactory nucleus) and posterior (bregma ~1.6 mm, hippocampal formation, cortex, thalamus and hypothalamus) contained signatures of both mature oligodendrocytes and OPCs, but in different proportions (Fig. 2d, compare sections 3–6). This result suggests a relative enrichment of mature oligodendrocytes in the posterior section compared with the anterior section. We hypothesized that this difference in cell-type composition reflects the functional properties of the associated brain regions. In particular, mature oligodendrocytes are responsible for producing myelin, a lipid-based material that sheaths and insulates nerve axons throughout the central nervous system[26,27]. In particular, we observed increased white matter regions (for example, corpus callosum) and other fiber tracts in the posterior section, and we thus sought to investigate if mature oligodendrocytes comprise a higher proportion of oligodendrocyte-lineage cells in white-matter tracts versus cortical regions.

PSS compares cell composition between brain regions

To test if the observed differences in oligodendrocyte-lineage cell composition between anterior and posterior tissues sections could be explained by tissue composition, we applied PSS to examine oligodendrocyte-lineage cells within white and gray matter subregions of a coronal brain section. Specifically, we generated ATAC-seq profiles for oligodendrocyte-lineage cells within the corpus callosum, a connective white matter region consisting of millions of myelinated axons, and the cortex, the outermost gray matter layer of the brain (Fig. 2e and Extended Data Fig. 2h). To do this, we collected tissue sections from the mouse hippocampus, which were stained for OLIG2 and processed according to the in situ library generation phase of the PSS protocol (Fig. 1a, step 1). During the imaging stage, we acquired whole-section scans to visualize the overall tissue morphology and identify the cortex and corpus callosum regions. We targeted oligodendrocyte-lineage cells in either the cortex ($n = 4$ biological replicates, each with approximately 770 selected cells) or corpus callosum ($n = 2$ tissue sections, each with approximately 650 selected cells) during the selective illumination phase (Fig. 1a, step 2), and proceeded through sequencing (results listed in Supplementary Table 1).

We compared the corpus callosum and cortex oligodendrocyte-lineage cell profiles with the scATAC-seq data by calculating the cisTopic z-score correlations as described above (Fig. 2d, sections 7 and 8). As expected, we found that both brain regions contain signatures of mature oligodendrocytes and OPCs. However, oligodendrocyte-lineage cells from the corpus callosum region correlated more strongly with mature oligodendrocytes, consistent with our previous observation. To expand on this result, we leveraged the scATAC-seq data to decompose the PSS oligodendrocyte-lineage cell accessibility

Fig. 2 | PSS robustly reproduces aggregate single-cell ATAC data and characterizes the regional composition of oligodendrocyte-lineage cells in the mouse brain. a, Morphologically guided selection of specific cell types in the mouse brain. The dentate gyrus granule cells are resident to a characteristic v-shape region in the mouse hippocampus (top). OLIG2 immunofluorescence marks oligodendrocyte-lineage cells (bottom). **b**, Example images show target ROIs for the dentate gyrus, identified using a DRAQ5 DNA stain (purple), and oligodendrocyte-lineage cells, identified using OLIG2 immunofluorescence (green). Yellow (granule cells) or red (oligodendrocyte-lineage cells) outlines indicate targeted cells. Coverage traces (right) compare the PSS ATAC-seq profiles (bottom traces; PSS) to aggregated scATAC-seq profiles for the corresponding cell types (top traces; SC) at example marker gene loci. **c**, UMAP plot showing clustering of reference scATAC-seq data on cisTopic z-score. **d**, Heat map shows pairwise Pearson correlation coefficients of the cisTopic z-scores for the PSS data and aggregate scATAC-seq profiles. Red text indicates pseudobulk scATAC-seq data corresponding to a PSS-targeted cell type. Schematic diagram shows brain region for PSS samples. **e**, PSS compares oligodendrocyte-lineage cells in the cortex and corpus callosum. Schematic inserts indicate the corpus callosum and cortex regions of the hippocampus, while images show example target oligodendrocyte-lineage nuclei within the specified region. **f**, Bar graph of cell-type-decomposition results indicates that the oligodendrocyte-lineage cell population is relatively enriched for mature oligodendrocytes in white-matter dense (posterior) and pure white matter regions (corpus).

profiles by cell type. To do this, we performed stepwise linear regression on the cisTopic *z*-scores with the pseudobulk scATAC-seq profiles as independent variables (approach and validation described in 'Stepwise linear regression' section in Methods; Extended Data Fig. 2i). The regression coefficients were taken as the proportions of the constituent cell types in the PSS oligodendrocyte-lineage cell data.

We found that mature oligodendrocytes account for 73% of the oligodendrocyte-lineage cell population in posterior tissue sections compared with 47% in anterior tissue sections. This effect intensifies in pure gray and white matter regions, where we estimate that 86% of corpus callosum oligodendrocyte-lineage cells are mature oligodendrocytes, compared with 47% in the cortex (Fig. 2f).

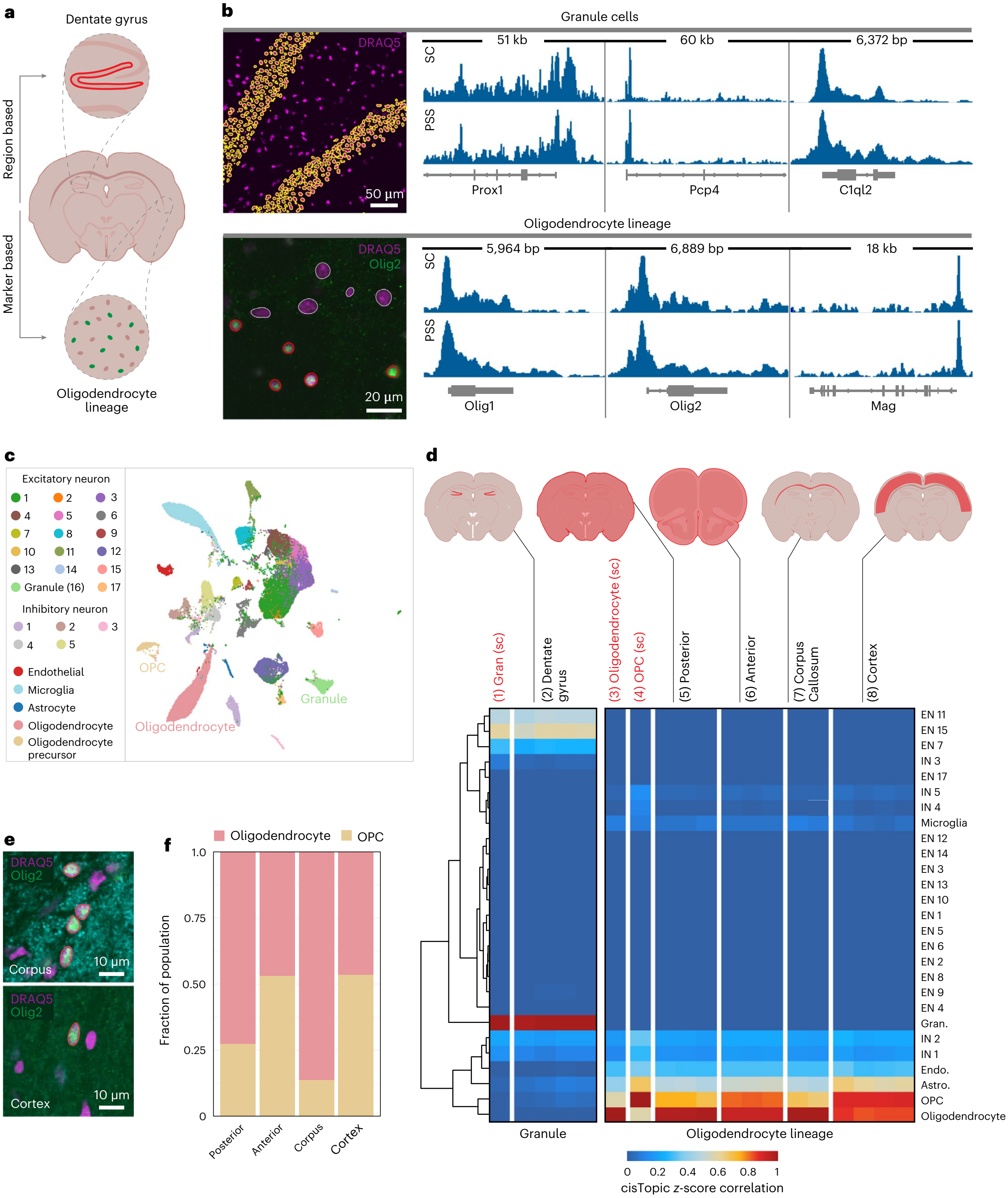

Notably, previous studies have demonstrated that OPCs localize roughly evenly throughout the brain, and furthermore that mature oligodendrocytes are densely packed within the corpus callosum region[28]. Therefore, the fractional populations of oligodendrocytes and OPCs we have calculated for gray and white matter regions are in line with expectation, and demonstrate that PSS sensitively detects distinct epigenomic profiles within specific regions of the mouse brain. Furthermore, our method for co-analyzing the PSS data with existing scATAC-seq atlases enables decomposition of the bulk PSS accessibility profile into the contributions of individual cell types. Using this combined experimental and computational framework we demonstrate that PSS can infer the spatial distribution of specific cell types across tissue regions.

PSS assays genomic sequences at the nuclear periphery

We next sought to define subcellular structures using PSS. The nuclear periphery is a key structural component of the nucleus known to play an important role in genome organization and gene regulation[29–31]. Furthermore, misregulation of interactions between the genome and the nuclear periphery have been implicated in age-related disorders and disease[30]. Therefore, a comprehensive understanding of the features that influence genome–nuclear periphery interactions would elucidate basic biological principles and have relevance in the context of human well-being. Previous studies have investigated specific protein–DNA interactions at the nuclear periphery, and in particular identified hundreds of lamin-associated domains (LADs) that range from 0.1 to 10 Mb in size[32]. Typically, these domains are defined by profiling Lamin B1–DNA interactions, either by proximity labeling assays or by chromatin immunoprecipitation followed by high-throughput sequencing (ChIP–seq)[33–36]. However, these assays measure specific protein–DNA interactions and do not probe all sequences at the nuclear periphery in an unbiased manner. Using PSS, we selectively sequence the DNA at the nuclear periphery. We compare our results with published lamin B1 ChIP–seq data[37] while exploring general features of peripheral DNA.

We constructed PSS libraries in adherent human fibroblast cells (IMR90) cells that were previously immunostained against Lamin B1 as a marker for the nuclear periphery (Fig. 3a, green), with an important modification. Specifically, we performed whole genome tagmentation by using a gentle histone disruption treatment to facilitate unbiased Tn5 transposase insertion across all chromatin states ('Histone denaturing treatment' section in Methods)[38]. During the photoselection phase, we unblocked DNA fragments at the nuclear periphery ($n = 3$ biological replicates, each with approximately 2,000 selected cells; Supplementary Table 1), defined as the two-dimensional boundary of the nucleus in the focal plane where the nuclear area is maximized (Fig. 3a (yellow outlines) and 'Photoselection' section in Methods). The purified libraries from each sample were split into paired halves, one of which was prepared as an input library by uncaging all constituent fragments before secondary-adapter ligation ('Reverse crosslinking and library purification' in Methods). This enables enrichment-based measurements during the analysis stage ('Enrichment traces' section in Methods). Preliminary analysis of the sequencing data showed that PSS detects an average of 33,819 unique fragments per selected nuclear periphery (or 96,300 fragments per 100 μm^2 of selected area for whole genome libraries in IMR90 cells; Extended Data Fig. 3a and Supplementary Table 1).

Peripheral enrichment trends inversely with chromosome size

We first asked which chromosomes are most enriched for reads in the PSS and ChIP–seq data ('Enrichment traces' section in Methods). We found that the enrichments are generally inversely correlated with chromosome length, consistent with previous observations that the larger chromosomes are more peripheral on average (Fig. 3b)[39,40]. However, there is a clear discrepancy between the PSS and ChIP–seq enrichments for chromosomes 13–15, 19, 21 and 22. Notably, with the exception of chromosome 19, these chromosomes each harbor nucleolar organizing regions, and thus interact with the nucleoli (Fig. 3b, starred). Besides having a key structural role in the nuclear lamina, lamin B1 protein is present throughout the nucleoplasm (Fig. 3a, green) and contributes to nucleolar organization[41]. The relatively higher ChIP–seq enrichment for these chromosomes may stem from interactions with nucleoplasmic and nucleolar lamin B1 protein, which do not occur at the periphery and are not detected by PSS. To remove the effects of chromosome positioning, the lamin B1 ChIP–seq and PSS profiles are normalized on a per chromosome basis for all further computation.

PSS characterizes features of peripheral chromatin

We next compared the lamin B1 ChIP–seq and PSS profiles genome wide. To do this, we calculate the log-fold enrichment along the coordinates of the genome using a 100 kb bin size (Fig. 3c, Extended Data Fig. 4 and 'Enrichment traces' section in Methods). We selected this bin size because it is on the scale of the smallest LADs, and because replicate PSS profiles were strongly correlated using this binning (Extended Data Fig. 3b). We observe that the PSS and ChIP–seq profiles display many shared features and are strongly correlated ($r = 0.62$ on average) genome wide (Fig. 3c,d). Notable exceptions include chromosomes 4 and 5, which show a relatively low correlation ($r = 0.44$ and 0.45, respectively). Upon further investigation, we found that the PSS profiles for these chromosomes are strongly correlated with positioning along the chromosome, with depletion in the p-arm and enrichment in the q-arm (Fig. 3d and Extended Data Fig. 4). One potential explanation for this effect is that these chromosomes are polarized such that the p-arms are oriented towards the nuclear interior on average, and thus less likely to interact with the periphery. Alternatively, the p-arms of these chromosomes may interact with the 3D surface of the nuclear lamina, but not the 2D border.

The molecular mechanisms that regulate chromatin association with the nuclear periphery are only beginning to emerge[29]. However, it has been observed that lamin-associated chromatin is enriched for repressive histone modifications. Of particular importance, H3K9me2 and H3K9me3 are hypothesized to structure and maintain LADs through their interaction with the nuclear lamina, either directly or through the action of an intermediary protein[29,42,43]. To further investigate the interplay between chromatin features and genome organization, we asked which histone modifications are characteristic of peripheral chromatin regardless of LAD membership. Using the ENCODE database[44], we analyzed all available histone modification ChIP–seq profiles that were collected from IMR90 cells. Binned enrichments were calculated for the ENCODE data ('Enrichment traces' section in Methods), and correlated with the PSS data ('Correlation analysis' section in Methods). We note that all obtained data were derived from active chromatin marks, with the exception of the H3K9me3 profile. Consistent with previous observations, we find that the PSS profile is positively correlated with the repressive mark H3K9me3 ($r = 0.47$), and negatively correlated with the active marks (Fig. 3d).

Given that H3K9me3 plays a known role in LAD formation, we asked if peripheral chromatin outside of LADs is also enriched for this histone modification. To do this, we regressed the lamin B1 ChIP–seq profile out of the PSS profile ('Correlation analysis' section in Methods) and quantified the residuals. We found that the H3K9me3 repressive mark was still correlated with the PSS residuals, even after removing the correlation with lamin B1 (Extended Data Fig. 3c). To validate our findings, we visualized the spatial localization of H3K9me3 using immunofluorescence (Fig. 3e). We calculated the radial intensity profile of the fluorescent marker, and found a relative enrichment at the nuclear periphery as expected (Fig. 3f, Extended Data Fig. 3d and 'Radial intensity profiles' section in Methods). Correspondingly, we calculated the radial enrichment of H4K8ac and H4K20me, two histone marks binding profiles that were anti-correlated with the PSS nuclear periphery data

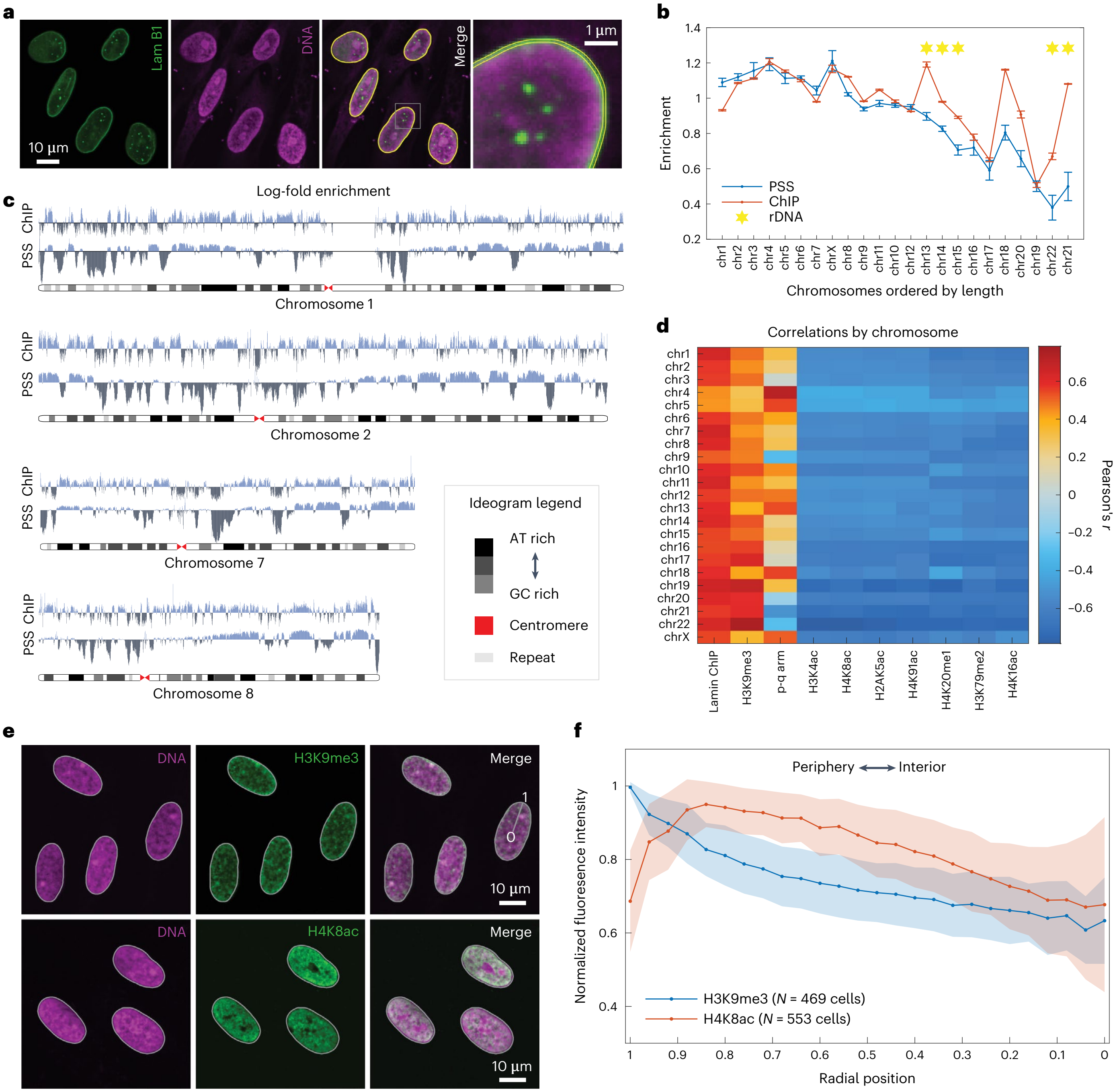

Fig. 3 | PSS identifies features of chromatin at the nuclear periphery. **a**, Images show lamin immunostain (green), an unbiased PSS library (magenta) and the merged image. Yellow outlines indicate the nuclear periphery region. Enlarged image illustrates the 300-nm-thick target region. **b**, Images shown are from a single experiment PSS nuclear periphery profile compared with a published LamB ChIP-seq at the chromosome level (chromosomes ordered by length). Plot shows fold enrichment for PSS or ChIP–seq compared with an input (untargeted) library. Error bars represent the s.d. about the mean (two ChIP–seq replicates, three PSS replicates examined over two experiments). Yellow stars indicate chromosomes containing ribosomal DNA (rDNA) repeats. **c**, Log-fold enrichment profiles for nuclear periphery PSS and LamB ChIP–seq for a subset of chromosomes (for all chromosomes, see Extended Data Fig. 4). Profiles are pooled across replicates. **d**, Heat map correlates PSS profiles with ChIP–seq profiles of histone modifications from the ENCODE database on a per chromosome basis. Chromosome 4–5 profiles are particularly correlated with distance from the centromere (Extended Data Fig. 4), and all chromosomes show a positive correlation with the H3K9me3 ChIP–seq profile. **e**, Images showing immunostaining of H3K9me3 and H4K8ac, which are histone marks having ChIP–seq profiles that are correlated and anti-correlated with the PSS nuclear periphery profile, respectively. **f**, Radial fluorescence intensity profiles for H3K9me3- and H4K8ac-labeled cells. Solid lines represent mean normalized fluorescence intensity (Methods) for H3K9me3 (*N* = 569 cells, 1 experiment) or H4K8ac (*N* = 553 cells, 1 experiment). The shaded region indicates 1 s.d.

(Fig. 3d and Extended Data Fig. 3e). As expected, we found a relative depletion of these histone marks at the nuclear periphery. Overall, our results suggest that H3K9me3-marked chromatin preferentially localizes to the nuclear periphery, even without direct lamin B interaction. Moreover, these results demonstrate that PSS is able to probe subcellular nuclear organization, and sample orthogonal and complementary spatial relationships as compared with ChIP–seq, which samples molecular interactions.

Discussion

PSS is a new method that assimilates imaging and sequencing data by enabling genomic or epigenetic sequencing measurements within specific ROIs, as visualized by fluorescence microscopy. We demonstrate that PSS flexibly applies across ROIs that span order-of-magnitude size scales, from entire regions of the mouse brain to the nuclear periphery in IMR90 cells. In-line image segmentation enables ROI generation based on an extensive range of spatial features and automates the targeted illumination process over large numbers of cells or features. At the cellular scale, PSS reveals that OPCs account for a relatively high proportion of oligodendrocyte-lineage cell population in the cortex compared with the corpus callosum. At the subcellular scale, we selectively sequence the nuclear periphery and demonstrate that the PSS data are consistent with published lamin B1 ChIP–seq data, while also revealing H3K9me3-marked chromatin is enriched at the periphery regardless of laminB1 interaction. Taken together, these results demonstrate that PSS has the potential to uncover new connections between spatial and genomic information at diverse length scales.

We anticipate that PSS will be a useful tool for fast, sensitive and robust spatial annotation of cell types and states. In contrast to RNA, DNA is compartmentalized into a cell's nucleus providing defined boundaries that are easily identified and well suited for photoselection. Further, PSS requires the deprotection of two oligonucleotides, which reduces background signal. Finally, large-scale scATAC-seq efforts are underway to create a catalog of accessible regions of the genome, which reflect highly cell-type-specific signatures of cell types and states[45]. We demonstrate this by combining a scATAC-seq atlas with PSS to assess the spatial distribution of cell types within the mouse brain. To do this, we establish a computational strategy which uses topics from scATAC-seq data to deconvolve spatial PSS bulk data. Future work may improve upon this strategy by leveraging recent advancements of bulk sample deconvolution[46].

It is difficult to directly compare PSS with other methods that use light to perform selective measurements in visually identified populations of cells because these methods apply to transcriptomics and have not produced genomic or epigenomic data. However, we compare PSS with recently developed array-based spatial genomic and epigenomic methods that enable genome-wide profiling of tissue sections[47–50]. These methods typically offer 10–50 µm spatial resolution and capture 400–3,000 fragments within a 100 µm^2 area, depending on the method, tissue type and library preparation (for example, ~1,900 fragments per 100 µm^2 for spatial ATAC-seq[47] and ~3,000 fragments per 100 µm^2 for slide DNA-seq[49]). PSS is more sensitive than these techniques with an average detection rate of 3,846 fragments per 100 µm^2 for ATAC-seq libraries and 96,254 fragments per 100 µm^2 for whole genome libraries. Although it is not straightforward to define an overall spatial resolution for PSS, we are able to select regions that range in size from millimeters down to 300 nm (Extended Data Fig. 1c), and with higher genomic sampling than existing methods.

Compared with PSS, existing spatial genomics and epigenomics methods can be inaccessible due to cost, reagent availability and difficulty of implementation. For example, array-based spatial barcoding methods powerfully profile large numbers of cells in tissue sections, but require the use of specialized microfluidics or custom arrays. Furthermore, because library generation is not targeted to a population of interest, sequencing costs can be extremely high (even for an individual tissue section), and deep sequencing is required to adequately profile uncommon cell types or smaller spatial regions. PSS only requires common reagents and a suitable imaging system. We expect that an appropriate imaging system will be available in most microscopy cores, and note that photoselection may be accomplished using a variety of devices including laser-scanning confocal microscopes, targeted-illumination devices and digital micromirror devices. Furthermore, PSS reduces sequencing costs by targeting library generation to the cellular population of interest, which decreases the number of reads needed to adequately profile the sample. Altogether, we believe that PSS balances usability of the method with information content in the resulting data and is a strong addition to the range of available spatial genomics tools.

One limitation of the current PSS protocol is that only a single set of spatial regions can be selected within each specimen, and the data are inherently aggregate over these ROIs. Although this drawback can partially mitigated by deconvolution algorithms, future versions of PSS may enable spatial barcoding of multiple classes of (and potentially individual) spatial regions. Potential approaches for multiplexed target selection include the use of pooled tagmentation adapters that uncage upon exposure to spectrally distinct wavelengths of light, or subsequent rounds of photoselection and barcode ligation in situ. Furthermore, we do not currently recommend PSS for applications that require 3D photoselection, such as targeting small ROIs within the nuclear interior. This is because the targeted illumination laser passes through the entire thickness of specimen and can uncage fragments above and below the focal plane. At this time, we navigate this effect by sectioning tissues to approximately single-cell thickness, and optimizing optical conditions. Both the axial and lateral resolution of the method could be markedly improved by uncaging the library with two-photon absorption, enabling fully volumetric photoselection.

The PSS library preparation is compatible with numerous genomic and epigenomic measurements. For example, the in situ library preparation stage may be compatible with multiple tagmentation strategies (provided that the transposase carries the photocaged adapters), and we have already documented construction of both ATAC and unbiased whole genome libraries here. An avenue for future exploration would be to generate protein-targeted fragment libraries using a recently described strategy where proteinA–Tn5 transposase fusion is anchored to the target protein via a specific antibody, resulting in site-specific tagmentation of the underlying chromatin[19,20]. Using photoselection would restrict profiling to specific ROIs, such as particular nuclei, or even subcellular regions. Overall, we expect that the library preparation and downstream analysis phases may be tailored to a wide variety of biological applications. In summary, PSS is a novel spatial genomic method that applies across a diverse range of cell types and species, and is straightforwardly adaptable to accommodate numerous genomic and epigenomic measurements. By combining imaging- and sequencing-based readouts PSS will uncover new connections at the interface of physical and genomic space. We expect that the user-friendly protocol and lack of specialized materials will facilitate uptake throughout the research community.

Online content

Any methods, additional references, Nature Portfolio reporting summaries, source data, extended data, supplementary information, acknowledgements, peer review information; details of author contributions and competing interests; and statements of data and code availability are available at https://doi.org/10.1038/s41592-023-01845-8.

References

1. Zheng, H. & Xie, W. The role of 3D genome organization in development and cell differentiation. *Nat. Rev. Mol. Cell Biol.* **20**, 535–550 (2019).
2. Misteli, T. Beyond the sequence: cellular organization of genome function. *Cell* **128**, 787–800 (2007).
3. Schneider, R. & Grosschedl, R. Dynamics and interplay of nuclear architecture, genome organization, and gene expression. *Genes Dev.* **21**, 3027–3043 (2007).
4. Misteli, T. Concepts in nuclear architecture. *Bioessays* **27**, 477–487 (2005).
5. Strom, A. R. et al. Phase separation drives heterochromatin domain formation. *Nature* **547**, 241–245 (2017).

6. Higgs, D. R. Enhancer–promoter interactions and transcription. *Nat. Genet.* **52**, 470–471 (2020).
7. Wainwright, E. N. & Scaffidi, P. Epigenetics and cancer stem cells: unleashing, hijacking, and restricting cellular plasticity. *Trends Cancer Res.* **3**, 372–386 (2017).
8. Mohammad, H. P. & Baylin, S. B. Linking cell signaling and the epigenetic machinery. *Nat. Biotechnol.* **28**, 1033–1038 (2010).
9. Arzate-Mejía, R. G., Valle-García, D. & Recillas-Targa, F. Signaling epigenetics: novel insights on cell signaling and epigenetic regulation. *IUBMB Life* **63**, 881–895 (2011).
10. Lovatt, D. et al. Transcriptome in vivo analysis (TIVA) of spatially defined single cells in live tissue. *Nat. Methods* **11**, 190–196 (2014).
11. van der Leun, A. M. et al. Single-cell analysis of regions of interest (SCARI) using a photosensitive tag. *Nat. Chem. Biol.* **17**, 1139–1147 (2021).
12. Hu, K. H. et al. ZipSeq: barcoding for real-time mapping of single cell transcriptomes. *Nat. Methods* **17**, 833–843 (2020).
13. Genshaft, A. S. et al. Live cell tagging tracking and isolation for spatial transcriptomics using photoactivatable cell dyes. *Nat. Commun.* **12**, 1–15 (2021).
14. Kishi, J. Y. et al. Light-Seq: light-directed in situ barcoding of biomolecules in fixed cells and tissues for spatially indexed sequencing. *Nat. Methods* **19**, 1393–1402 (2022).
15. Emmert-Buck, M. R. et al. Laser capture microdissection. *Science.* **274**, 998–1001 (1996).
16. Lipovsek, M. et al. Patch-seq: past, present, and future. *J. Neurosci.* **41**, 937–946 (2021).
17. Tang, F. et al. mRNA-seq whole-transcriptome analysis of a single cell. *Nat. Methods* **6**, 377–382 (2009).
18. Buenrostro, J. D., Wu, B., Chang, H. Y. & Greenleaf, W. J. ATAC-seq: a method for assaying chromatin accessibility genome-wide. *Curr. Protoc. Mol. Biol.* **109**, 21.29.1–21.29.9 (2015).
19. Carter, B. et al. Mapping histone modifications in low cell number and single cells using antibody-guided chromatin tagmentation (ACT-seq). *Nat. Commun.* **10**, 1–5 (2019).
20. Kaya-Okur, H. S. et al. CUT&Tag for efficient epigenomic profiling of small samples and single cells. *Nat. Commun.* **10**, 1–10 (2019).
21. Buenrostro, J. D., Giresi, P. G., Zaba, L. C., Chang, H. Y. & Greenleaf, W. J. Transposition of native chromatin for fast and sensitive epigenomic profiling of open chromatin, DNA-binding proteins and nucleosome position. *Nat. Methods* **10**, 1213–1218 (2013).
22. Chen, X. et al. ATAC-see reveals the accessible genome by (v2.29.2)-mediated imaging and sequencing. *Nat. Methods* **13**, 1013–1020 (2016).
23. Sinnamon, J. R. et al. The accessible chromatin landscape of the murine hippocampus at single-cell resolution. *Genome Res.* **29**, 857–869 (2019).
24. Lareau, C. A. et al. Droplet-based combinatorial indexing for massive-scale single-cell chromatin accessibility. *Nat. Biotechnol.* **37**, 916–924 (2019).
25. Bravo González-Blas, C. et al. cisTopic: cis-regulatory topic modeling on single-cell ATAC-seq data. *Nat. Methods* **16**, 397–400 (2019).
26. Kuhn, S., Gritti, L., Crooks, D. & Dombrowski, Y. Oligodendrocytes in development, myelin generation and beyond. *Cells* **8**, 1424 (2019).
27. Bradl, M. & Lassmann, H. Oligodendrocytes: biology and pathology. *Acta Neuropathol.* **119**, 37–53 (2010).
28. Rivers, L. E. et al. PDGFRA/NG2 glia generate myelinating oligodendrocytes and piriform projection neurons in adult mice. *Nat. Neurosci.* **11**, 1392–1401 (2008).
29. Buchwalter, A., Kaneshiro, J. M. & Hetzer, M. W. Coaching from the sidelines: the nuclear periphery in genome regulation. *Nat. Rev. Genet.* **20**, 39–50 (2018).
30. Mekhail, K. & Moazed, D. The nuclear envelope in genome organization, expression and stability. *Nat. Rev. Mol. Cell Biol.* **11**, 317–328 (2010).
31. Van de Vosse, D. W., Wan, Y., Wozniak, R. W. & Aitchison, J. D. Role of the nuclear envelope in genome organization and gene expression. *Wiley Interdiscip. Rev. Syst. Biol. Med.* **3**, 147–166 (2011).
32. Guelen, L. et al. Domain organization of human chromosomes revealed by mapping of nuclear lamina interactions. *Nature* **453**, 948–951 (2008).
33. Pickersgill, H. et al. Characterization of the *Drosophila melanogaster* genome at the nuclear lamina. *Nat. Genet.* **38**, 1005–1014 (2006).
34. Sadaie, M. et al. Redistribution of the Lamin B1 genomic binding profile affects rearrangement of heterochromatic domains and SAHF formation during senescence. *Genes Dev.* **27**, 1800–1808 (2013).
35. Shah, P. P. et al. Lamin B1 depletion in senescent cells triggers large-scale changes in gene expression and the chromatin landscape. *Genes Dev.* **27**, 1787–1799 (2013).
36. Lund, E., Oldenburg, A. R. & Collas, P. Enriched domain detector: a program for detection of wide genomic enrichment domains robust against local variations. *Nucleic Acids Res.* **42**, e92 (2014).
37. Dou, Z. et al. Autophagy mediates degradation of nuclear lamina. *Nature* **527**, 105–109 (2015).
38. Beliveau, B. J. et al. Single-molecule super-resolution imaging of chromosomes and in situ haplotype visualization using Oligopaint FISH probes. *Nat. Commun.* **6**, 1–13 (2015).
39. Payne, A. C. et al. In situ genome sequencing resolves DNA sequence and structure in intact biological samples. *Science* **371**, e3446 (2021).
40. Bolzer, A. et al. Three-dimensional maps of all chromosomes in human male fibroblast nuclei and prometaphase rosettes. *PLoS Biol.* **3**, e157 (2005).
41. Martin, C. et al. Lamin B1 maintains the functional plasticity of nucleoli. *J. Cell Sci.* **122**, 1551–1562 (2009).
42. Towbin, B. D. et al. Step-wise methylation of histone H3K9 positions heterochromatin at the nuclear periphery. *Cell* **150**, 934–947 (2012).
43. Poleshko, A. et al. Genome-nuclear lamina interactions regulate cardiac stem cell lineage restriction. *Cell* **171**, 573–587.e14 (2017).
44. Moore, J. E. et al. Expanded encyclopaedias of DNA elements in the human and mouse genomes. *Nature* **583**, 699–710 (2020).
45. Corces, M. R. et al. Lineage-specific and single-cell chromatin accessibility charts human hematopoiesis and leukemia evolution. *Nat. Genet.* **48**, 1193–1203 (2016).
46. Newman, A. M. et al. Determining cell type abundance and expression from bulk tissues with digital cytometry. *Nat. Biotechnol.* **37**, 773–782 (2019).
47. Deng, Y. et al. Spatial profiling of chromatin accessibility in mouse and human tissues. *Nature* **609**, 375–383 (2022).
48. Deng, Y. et al. Spatial-CUT&Tag: spatially resolved chromatin modification profiling at the cellular level. *Science* **375**, 681–686 (2022).
49. Zhao, T. et al. Spatial genomics enables multi-modal study of clonal heterogeneity in tissues. *Nature* **601**, 85–91 (2021).
50. Foster, D. S. et al. Integrated spatial multiomics reveals fibroblast fate during tissue repair. *Proc. Natl Acad. Sci. USA* **118**, e2110025118 (2021).

Publisher's note Springer Nature remains neutral with regard to jurisdictional claims in published maps and institutional affiliations.

Springer Nature or its licensor (e.g. a society or other partner) holds exclusive rights to this article under a publishing agreement with the author(s) or other rightsholder(s); author self-archiving of the accepted manuscript version of this article is solely governed by the terms of such publishing agreement and applicable law.

© The Author(s), under exclusive licence to Springer Nature America, Inc. 2023

Methods

Animal handling

Animal procedures conducted at the Broad Institute complied with the US National Institute of Health Guide for the Care and Use of Laboratory Animals under protocol number 0211-06-18. We housed C57BL/6 mice (Charles River Laboratory) using a 12:12 light–dark cycle with ad libitum access to food and water. The average temperature was 21 ± 2 °C with 40 ± 10% humidity.

Tissue and cell preparation

Mouse brains were either prepared in-house (dentate gyrus experiment) or purchased by special request from Zyagen (all other experiments). Purchased brains were obtained from phosphate-buffered saline (PBS)-perfused adult mice and shipped flash frozen in accordance with Zyagen's protocols. Mouse perfusion, cell culture and tissue sectioning followed standard protocols as described in the following Supplementary Methods sections: 'Mouse perfusion', 'Cell culture' and 'Tissue sectioning'.

General notes

PSS uses glass-bottom well plates, which support both imaging and enzymatic steps (for example, Greiner 655892). Importantly, plates with black well dividers reduce light scattering and avoid cross-talk during the photoselection stage, and we find that 96- and 24-well formats are suitable for cultured cells and tissue sections, respectively. Unless otherwise specified, we use 100 µl (cells) or 400 µl (tissue) of buffer per well for wash steps, and 50 µl (cells) or 250 µl (tissues) of solution per well for enzymatic steps. Any solutions or samples containing the photocleavable adapters (Extended Data Table 1; PSS1 and PSS2) should be protected from light whenever possible. Finally, we recommend that each PSS experiment include at least one control sample that will not be exposed to targeted illumination and sequenced as a negative control.

Fixation and permeabilization

Cells were rinsed once in 1× PBS to remove excess growth medium, then fixed in 1% methanol-free paraformaldehyde (Electron Microscopy Sciences 15714) in 1× PBS for 10 min at room temperature. Excess fixative was removed by 3 × 5 min washes in 1× PBS. Cells were permeabilized in 0.5% Triton X-100 (Sigma 93443) in 1× PBS for 10 min at room temperature, then washed 3 × 5 min in 1× PBS.

Tissue sections were covered in 1% methanol-free paraformaldehyde (Electron Microscopy Sciences 15714) in 1× PBS for 10 min at room temperature. The fixation reaction was quenched by incubating in 250 mM Tris–HCl 8 (Invitrogen 15568) in 1× PBS for 5 min at room temperature. The tissue is washed 3 × 5 min in 1× PBS. It was then permeabilized with 0.5% Triton X-100 (Sigma 93443-100) in 1× PBS for 20 min, and washed again three times for 5 min. Fixed and permeabilized tissue was stored at 4 °C in 1× PBS until use.

Histone denaturing treatment

For unbiased libraries (nuclear periphery experiment), we gently denatured the histones by treating with 0.1 N HCl (Sigma H9892) diluted in water for 5 min at room temperature, then washed 3 × 5 min in 1× PBS[38]. This step should be completed before immunofluorescence, and is not used for ATAC-seq libraries. A loss of sensitivity to histone positioning is confirmed by observing a unimodal insert size distribution (Extended Data Fig. 3f).

Immunofluorescence

We used standard immunofluorescence protocols to identify target ROIs as needed (described in 'Immunofluorescence' section in Supplementary Methods). Antibodies are listed in Extended Data Table 2, and all were used at a 1:200 dilution. All antibodies in this study were obtained commercially, and validated by ensuring that the cellular localization was consistent with the images provided by the manufacturer.

Anneal adapters

Photocaged tagmentation adapters (Extended Data Table 1; PSS1 and PSS2) and the blocked mosaic end (Extended Data Table 1; PSS3) were obtained from Integrated DNA Technologies and resuspended in ultrapure water (Invitrogen 10977015) to a final concentration of 100 µM. The mosaic end sequence was annealed to the adapters using the following reaction: 25 µM PSS1, 25 µM PSS2, 50 µM PSS3, 10 mM Tris–HCl pH 8.0 and 50 mM NaCl. The annealing reaction was placed in a thermocycler, and the temperature was ramped from 85 °C to 20 °C over approximately 1 h. Annealed adaptors were mixed 1:1 with glycerol and stored at −20 °C until Tn5 loading.

Load Tn5 transposase

Tn5 transposase was purified in-house as previously described with a few modifications ('Transposase purification' section in Supplementary Methods)[51]. Annealed adapters were loaded into Tn5 transposase by combining the annealed adapters, Tn5 dilution buffer (50 mM Tris–HCl pH 7.5, 0.1 mM EDTA, 100 mM NaCl, 0.1% NP-40, 1 mM dithiothreitol and 50% glycerol) and 16.8 µM Tn5 transposase in a 2:1:1 ratio, then incubating for 30 min at room temperature. Loaded Tn5 was stored at −20 °C until use (for up to a few weeks).

In situ library preparation

Loaded Tn5 transposase was diluted 1:20 (cells) or 1:12 (tissues) in reaction buffer (0.3× PBS, 10 mM Tris pH 7.5, 5% dimethylformamide and 10 mM $MgCl_2$). The solution was applied to the samples, and the well plate was sealed with an adhesive film (Applied Biosystems 4306311), protected from light and incubated at 37 °C for 3 h. The transposition reaction was inactivated by replacing the reaction buffer with 50 mM EDTA in 1× PBS and incubating at 37 °C for 30 min. Samples were stained using 5 µM DRAQ5 (Abcam ab108410) in 1× PBS for 5 min and washed once with 1× PBS.

Imaging system

Imaging was performed using a Nikon Ti2-E inverted microscope equipped with a Yokogawa CSU-W1 confocal spinning disk unit and a Zyla 2.3 PLUS sCMOS camera. For confocal imaging we used 488 nm, 561 nm and 647 nm laser lines paired with 525/36 (MVI, 77074803), 582/15 (MVI, FF01-582/15-25) and 705/72 (MVI, 77074329) emission filters, respectively. For targeted illumination, the microscope was coupled to an XY galvo scanning module via the Ti2-LAPP system (Nikon), and we used a 50 mW 405 nm laser line. The 405 nm laser power at the objective was set to 1 mW. Samples were imaged through a 1.15 NA CFI Apo LWD Lambda S 40× water immersion objective lens (Nikon MRD77410). The imagining system was controlled by NIS-Elements AR software with the JOBS and General Analysis 3 (GA3) modules enabled.

Calibrating the targeted illumination module

Successful targeted illumination requires that (1) the targeted illumination laser is focused in the same plane as the confocal image, and (2) the position of the steering mirrors is correctly offset such that the beam precisely scans the on-screen ROIs. To ensure these conditions were met, we calibrated the targeted illumination system before each experiment as described in Supplementary Methods ('Calibrating the targeted illumination module').

Photoselection

The photoselection procedure is summarized as follows: for each relevant field of view within the sample (1) acquire a multichannel confocal image to visualize the fragment library and sample morphology, (2) manually or algorithmically define ROIs, (3) selectively illuminate the ROIs with near-UV light and (4) acquire a second confocal image to ensure successful cleavage of the PSS adapter, as indicated by loss of fluorescence (optional). We note that it is feasible to implement this process manually for selection of large spatial regions (for example, the dentate gyrus) but highly recommend a programmatic approach for more numerous regions, especially if they are distributed throughout the sample. Most commercial imaging systems with laser-scanning capabilities are controlled by software equipped with some degree of built-in image processing capabilities. In our hands, NIS Elements AR with the JOBS and GA3 modules enabled was best suited to PSS, and all photoselection was automated using these tools. The image-processing specifications quoted in the following sections are particular to the adjustable parameters in our Nikon software; however, the process is generalizable to other systems. All JOBS and GA3 scripts are available through GitHub (https://github.com/sarahmangiameli/pss-tools), and we explicitly list which scripts were used for each sample in Supplementary Table 1. The specific photoselection procedure for each experiment is detailed in Supplementary Methods ('Photoselection' section).

Reverse crosslinking and library purification

Samples were digested by incubation in reverse-crosslinking buffer (50 mM Tris pH 8, 50 mM NaCl and 0.2% SDS) with 1:50 proteinase K (NEB P8107S) for 8–16 h at 55 °C. The digestion buffer was added directly to the well plate, which was sealed with an adhesive film (Applied Biosystems 4306311) and protected from light. Digested samples were column purified using the NucleoSpin Gel and PCR Clean-Up kit (TaKaRa 740609) according to the manufacturer's directions, except we perform two successive rounds of elution using 20 µl then 16 µl of 10 mM Tris pH 8 (regardless of well size). At this stage, we optionally reserve half the eluate volume to create an input library to enable enrichment-based measurements as follows: (1) the eluate from each sample is split into two PCR tubes, each containing 16 µl of volume, (2) one of these tubes under a 365 nm LED (LED: Thorlabs M365LP1-C5, driver: Thorlabs LEDD1B, 0.15 mW mm^{-2} at sample) for 3 min such that all fragments become uncaged. Input libraries are then processed in the same manner as the photoselected libraries in all subsequent steps.

Adapter ligation

We ligate secondary adapters (Extended Data Table 1; PSS4 and PSS5) to the ends of uncaged fragments using splints (Extended Data Table 1 and Supplementary Table 2; PSS6 and PSS7) to stabilize the assembly (Fig. 1a (step 4) and Extended Data Fig. 1a). We first perform an annealing step to preassemble fragments by adding 4 µl of annealing master mix (2.5 µl of 10× T4 Ligase Buffer, 0.25 µl of ISS4, 0.25 µl of 100 µM ISS5, 0.25 µl of 100 µM ISS6 and 0.75 µl of water) to 16 µl of eluate from each sample. Finally, we add 2.5 µl of uniquely indexed ISS5 to each sample (total volume 22.5 µl) and perform the annealing by ramping the temperature from 50 °C to 43 °C for 10 min, then down to 25 °C, using a ramp rate of −0.1 °C s^{-1}. Once the temperature reaches 25 °C, we spike in 2.5 µl of 3 M U ml^{-1} T7 DNA ligase (NEB M0318L) and continue incubating for 1 h at 25 °C, followed by a 10 min at 65 °C and a 4 °C hold. The ligation reaction is purified by adding 25 µl of Ampure XP beads (Beckman Coulter A63880) to the reaction (1:1 ratio) and continuing the clean-up according to the manufacturer's directions. For elution, we add 23 µl of 10 mM Tris pH 8 to the beads and transfer 20 µl to a fresh PCR tube.

Library amplification and quantification

Libraries are amplified and quantified as described in Buenrostro et al.[18]. In summary, the 20 µl of eluate from the previous step was combined with 2.5 µl of 25 µM PSS8, 2.5 µl of 25 µM PSS9 and 25 µl of NEBNext High-Fidelity 2× PCR Master Mix (NEBM0541L). We cycle the PCR reaction using the following conditions: 72 °C for 5 min, 98 °C for 30 s, five cycles of 98 °C for 10 s then 72 °C for 1 min 30 s, 72 °C for 2 min, 4 °C hold. To determine the optimal number of additional PCR cycles using qPCR, we combine 5 µl of previously amplified DNA with 0.25 µl of 25 µM PSS8, 0.25 µl of 25 µM PSS9, 0.09 µl of 100× SYBR Green, 5 µl NEBNext High-Fidelity 2× PCR Master Mix and 4.41 µl of water (two technical replicates per sample). The qPCR program is as follows: 98 °C for 30 s, 20 cycles of 98 °C for 10 s, then 72 °C for 1 min 30 s, 72 °C for 1 min. The calculated number of additional cycles corresponds to the point where the relative fluorescence reaches 25–30% of the maximum value. The original partially amplified libraries were returned to the thermocycler for the calculated number of cycles (*N*) using the following program: 98 °C for 30 s, *N* cycles of 98 °C for 10 s, then 72 °C for 1 min 30 s, 72 °C for 2 min, 4 °C hold. PCR reactions were cleaned by adding 48 µl of Ampure XP beads (Beckman Coulter A63880) to the 40 µl reaction volume (1.2× ratio), then following the manufacturer's directions. Libraries were eluted in 20 µl of 10 mM Tris pH 8 and stored at −20 °C until quantification and sequencing.

Library quantification

Libraries were quantified via qPCR using the KAPA Library Quantification Kit (Roche 0796020400) according to the manufacturer's directions. The fragment length was obtained using a Bioanalyzer (Alegent) following the manufacturer's directions.

Sequencing

PSS libraries were designed using Illumina Nextera sequences and do not require custom primers. Libraries were sequenced on an Illumina Nextseq 500 using the following read structure: 60 bp read 1, 60 bp read 2, 20 bp index 1.

Sequencing alignment and preprocessing

Alignment and preprocessing steps were performed as described in Buenrostro et al.[21]. Briefly, sequenced fragments were trimmed for adapter sequences using a custom Python script (version 2.7.14) and aligned to either the mm10 or hg38 reference genomes using Bowtie2 (version 1.2.2)[52]. Bowtie was called with the default parameters, except '-X 2000' was set to allow alignment of fragments up to 2,000 bp. Aligned fragments were sorted by genomic position and filtered by mapping quality (MAPQ >30 retained) using samtools (version 1.9). Alignments to unlocalized and unplaced sequences, the Y chromosome and the mitochondrial DNA were excluded from downstream analysis. Duplicate reads were removed using the Picard tools MarkDuplicates function (http://broadinstitute.github.io/picard, version 2.20.7), which also provides an estimate for the calculated library size using the duplication rate. TSS enrichment scores were calculated for ATAC-seq libraries as previously described in Buenrostro et al.[21].

PSS performance metrics

PSS performance was quantified by measuring fraction of fragments that are unblocked within ROIs, the blocking efficiency of the photocaging mechanism, and the SNR. These measurements are described in detail in the following Supplementary Methods sections: 'Intensity decrease during uncaging', 'Blocking efficiency' and 'Signal-to-noise ratio'.

Smoothed coverage traces

Smoothed coverage traces (Figs. 1c and 2b) were generated as follows. For each paired-end alignment, reads on the forward strand were shifted by +4 bp and reads on the reverse strand were shifted by −5 bp to account for the 9 bp duplications generated by Tn5-transposase insertions[21,53]. To smooth the final coverage traces, fragments were extended by 150 bp on each end. Finally, the adjusted fragment positions were output as a bed file and the bedtools genomecov function (v2.29.2) was used to generate coverage traces for visualization[54].

cisTopic analysis

Cis-regulatory topics representing 200 distinct axes of biological variation were calculated on the counts matrix of previously published scATAC-seq data in the mouse brain using cisTopic (v3)[24,25], binarized and then used as custom annotations within chromVAR[55] to score oligodendrocyte PSS ATAC-seq counts using the same peak set. Correlation heat maps were generated by calculating the correlation of z-scores of each cisTopic between bulk replicates and pseudobulk clusters from the single-cell data using the pheatmap package.

Stepwise linear regression

Linear regression was performed using the lm function of the stats package in R with the most variable cisTopic z-scores of the pesudobulk scATAC-seq profiles of the annotated brain clusters used as independent variables for each bulk PSS ATAC-seq replicate. Variables for the best-performing model for each sample were selected through forward selection with a P value cutoff of 10^{-12} using the ols_step_forward_p function of the olsrr package in R. Nonnegative coefficients were normalized to add up to 1, and then replicates for each condition were averaged to come up with the final cell-type composition estimates.

For validation, we applied the decomposition algorithm to pseudobulk oligodendrocyte and OPC profiles from an independent scATAC-seq dataset[23]. We first applied the model to pure oligodendrocyte and OPC profiles (constructed from the test dataset), and found that the model correctly detects only these cell types (Extended Data Fig. 2i). We next decomposed known mixtures of oligodendrocytes and OPC profiles that mirror those calculated in Fig. 2f (73% oligodendrocyte:23% OPC and 47% oligodendrocyte:53% OPC). We found that the model consistently underestimates the size of the OPC population size (by ~10%) but provides a reasonable measure of the relative OPC and oligodendrocyte population sizes (Extended Data Fig. 2i).

LamB ChIP–seq

LamB1 ChIP–seq data were originally published in Dou et al. 2015 and obtained from the NCBI Gene Expression Omnibus (GEO) database under accession number GSE63440 (ref. 37). Two replicate LamB1-ChIP–seq and paired input libraries were downloaded and processed as described above ('Sequencing alignment and preprocessing'), except with minor modifications to accommodate single-end reads. Specifically, Bowtie2 was called with the default parameters, and in the filtering stage we removed the requirement that reads map in a proper pair.

Enrichment traces

For the nuclear periphery experiment (Fig. 3), each PSS and ChIP–seq replicate is associated with paired targeted and input libraries (processed as described above). To generate the chromosome level enrichment plot (Fig. 3b), the number of reads mapping to each assembled chromosome was queried by running the 'samtools idxstats' command on the filtered bam files (see 'Sequencing alignment and preprocessing'). The read depth for each library was taken as the sum of mapped reads across all assembled chromosomes. We normalized the reads per chromosome in the targeted and input libraries by read depth and reported the ratio of these quantities as the enrichment.

To generate enrichment traces (Fig. 3c), the genome was divided into 100 kb bins. Replicate targeted and input libraries were merged into a single bam. Raw read counts were generated for the targeted and input libraries using the chromVar 'getcounts' function to read the filtered bam files into the genomic bins[55]. Raw read counts were normalized by read depth on a per chromosome basis, where the chromosomal read counts were obtained using 'samtools idxstats'. An enrichment value for each bin is obtained by taking the ratio of the normalized read counts in the targeted and total libraries. The log (base 2) of the enrichment is displayed.

Correlation analysis

The relative p–q arm position track for correlation analysis (Fig. 3d) using 100 kb genomic bins is described above. Centromere regions were obtained from the University of California, Santa Cruz table browser, and the midpoints were called as the centromere position. For each chromosome, a relative p–q arm position was assigned to each bin by subtracting the centromere position from the bincenter position and normalizing the result by the chromosome length.

Histone modification ChIP–seq data (and associated inputs) collected in IMR90 cells were downloaded from the ENCODE database (encodeproject.org)[44]. Data were obtained as aligned reads (hg38 bam files), and all post-alignment filtering steps were applied (see 'Sequencing alignment and preprocessing'). Binned enrichment traces for the ENCODE data were calculated as described above ('Enrichment traces'). The H4k16ac ChIP–seq data[56] were obtained separately as FASTQs and processed using our pipeline ('Sequencing alignment and preprocessing').

The PSS enrichment trace was correlated with the LamB1 ChIP–seq trace, the relative p–q arm position trace and all of the histone modification enrichment traces on a per chromosome basis. Traces were retained for further consideration if (1) the magnitude of the chromosome-averaged Pearson correlation coefficient was at least 0.4 and (2) the magnitude of the Pearson correlation coefficient for at least one chromosome was greater than 0.6. All positively correlated traces that meet these conditions, as well as the seven most negatively correlated traces are ultimately displayed in the figure. All P values associated with correlation coefficients shown in the figure are significant. The PSS residuals were calculated using stepwise linear regression (MATLAB stepwiselm function), and then correlated with the histone modification ChIP–seq profiles as described above.

Radial intensity profiles

Separate wells of IMR90 cells were immunostained for histone marks H3K9me3, H4K8ac or H3K4me20 using an Alexa 488 secondary (Extended Data Table 2), and stained with DRAQ5 to visualize the nuclei. Single-plane images of the DRAQ5 and antibody stains were acquired using a 40× objective.

For image processing, we registered the images across the two fluorescence channels allowing only translation. We generated a binary mask of the nuclei by smoothing the DRAQ5 image using a three-pixel-radius Gaussian blur and then thresholding. For background subtraction, this initial binary mask was dilated by five pixels, and then inverted. The background intensity for each channel was taken as the median pixel value inside the background mask, and was subtracted from each pixel in the aligned images before radial-intensity analysis. To generate a final nuclear mask from the initial mask, we remove subnuclear-sized regions, regions touching the image border, and large regions that correspond to multiple nuclei (nuclei were generally well separated, and we did not implement an algorithm to detect boundaries between tightly packed nuclei).

Finally, we quantified the radial intensity of the fluorescently labeled histone mark normalized by the DNA content. To do this, we generated a series of concentric ring-like regions by successively eroding the nuclear mask (using a three-pixel-radius disk) and then subtracting the inner mask from the outer mask (Extended Data Fig. 3d). Within each concentric region, we calculated the normalized radial intensity for each cell as follows,

$$I_{\mathrm{norm},i} = \frac{1}{\max\left(I_{\mathrm{norm}}\right)} \times \left(\frac{I_{\mathrm{hist},i}}{I_{\mathrm{DNA},i}}\right)$$

where $I_{\mathrm{norm},i}$ is the normalized intensity in the ith radial region, I_{norm} is a vector containing the normalized intensity values for all radial regions, $I_{\mathrm{hist},i}$ is the summed pixel intensity of the histone immunofluorescence image inside in the ith radial region and $I_{\mathrm{DNA},i}$ is the summed pixel intensity of the DNA stain inside the ith radial region. The normalized pixel intensity inside each radial region was plotted against the normalized radial position, where the positions of the innermost and outermost regions were set to 0 and 1, respectively. To calculate an averaged radial intensity profile (for each histone mark) across all cells, we binned the relative radial positions (0.04 bin size) and averaged the intensity values within each bin.

Reporting summary

Further information on research design is available in the Nature Portfolio Reporting Summary linked to this article.

Data availability

All raw PSS sequencing data are available from the Sequence Read Archive under accession PRJNA938491 (cultured cell samples) and PRJNA938180 (mouse brain samples). Raw images corresponding to quantitative analyses in this study are available via Zenodo under the following: https://doi.org/10.5281/zenodo.7677794 (intensity decrease measurement), https://doi.org/10.5281/zenodo.7677827 (H3K9me3 radial intensity), https://doi.org/10.5281/zenodo.7677835 (H4K8ac radial intensity) and https://doi.org/10.5281/zenodo.7677868 (H4K20me radial intensity). scATAC-seq data (mouse hippocampus) from Sinnamon et al.[23] are available through GEO (https://www.ncbi.nlm.nih.gov/geo/) under the accession GSE118987. scATAC-seq data (whole mouse brain) from Lareau et al.[24] were acquired via the GEO under accession number GSE123581. Histone ChIP–seq data were obtained from the ENCODE encyclopedia[44] (https://www.encodeproject.org/) under the following accession numbers: ENCFF411NQX (H3K4ac), ENCFF039LQB and ENCFF966TQK (H4K8ac), ENCFF319QES (H2AK5ac), ENCFF048DVC (H4K91ac), ENCFF088QGG (H4K20me1), ENCFF083IVC and ENCFF640TNT (H3K79me1), ENCFF179YRO (H3K9me3), ENCFF704DVN (H3K27me3), ENCFF513JSZ (H2BK15ac), ENCFF672BWZ (H3K9me1), ENCFF048DVC (H4K91ac), ENCFF091RNK (H2BK5ac), ENCFF992CZO (H3K79me2) and ENCFF058SOP (H2AK9ac). The H4K16ac data[56] are available under GEO accession number GSE56307. Lamin B1 ChIP–seq data from Dou et al.[37] are available under GEO accession number GSE63440. Source data are provided with this paper.

Code availability

Analysis scripts from this study are available at https://github.com/sarahmangiameli/pss-tools.

References

51. Picelli, S. et al. Tn5 transposase and tagmentation procedures for massively scaled sequencing projects. *Genome Res.* **24**, 2033–2040 (2014).
52. Langmead, B. & Salzberg, S. L. Fast gapped-read alignment with Bowtie 2. *Nat. Methods* **9**, 357–359 (2012).
53. Berg, D. E., Schmandt, M. A. & Lowe, J. B. Specificity of transposon Tn5 insertion. *Genetics* **105**, 813–828 (1983).
54. Quinlan, A. R. & Hall, I. M. BEDTools: a flexible suite of utilities for comparing genomic features. *Bioinformatics* **26**, 841–842 (2010).
55. Schep, A. N., Wu, B., Buenrostro, J. D. & Greenleaf, W. J. chromVAR: inferring transcription-factor-associated accessibility from single-cell epigenomic data. *Nat. Methods* **14**, 975–978 (2017).
56. Rai, T. S. et al. HIRA orchestrates a dynamic chromatin landscape in senescence and is required for suppression of neoplasia. *Genes Dev.* **28**, 2712–2725 (2014).

Acknowledgements

We are grateful to J. Strecker for assistance with Tn5 transposase purification. We thank Z. Chiang for providing scripts for the generation of smoothed coverage traces, and for advice on computational methods. F.C. acknowledges support from NIH Early Independence Award (1DP5OD024583), the NHGRI (R01HG010647), the Burroughs Welcome Fund CASI award and the Merkin Institute. Many figure panels incorporated images generated with BioRender.com.

Author contributions

F.C., S.M. and H.C. conceived the study. S.M., H.C. and J.A.D designed and performed experiments. S.M., A.S.E. and D.L. analyzed the data. All authors contributed to the interpretation of the results. S.M. wrote the manuscript with input from F.C. and J.D.B. All authors reviewed and edited the manuscript. F.C. and J.D.B. provided funding, technical guidance and project oversight.

Competing interests

S.M., H.C. and F.C. are listed as inventors on a patent application related to PSS. J.D.B. holds patents related to ATAC-seq and is on the scientific advisory board for Camp4, Seqwell and Celsee. F.C. is a founder of Curio Biosciences. The remaining authors declare no competing interests.

Additional information

Extended data is available for this paper at https://doi.org/10.1038/s41592-023-01845-8.

Supplementary information The online version contains supplementary material available at https://doi.org/10.1038/s41592-023-01845-8.

Correspondence and requests for materials should be addressed to Jason D. Buenrostro or Fei Chen.

Peer review information *Nature Methods* thanks Yang Liu and the other, anonymous, reviewers for their contribution to the peer review of this work. Primary Handling Editor: Rita Strack, in collaboration with the *Nature Methods* team.

Reprints and permissions information is available at www.nature.com/reprints.

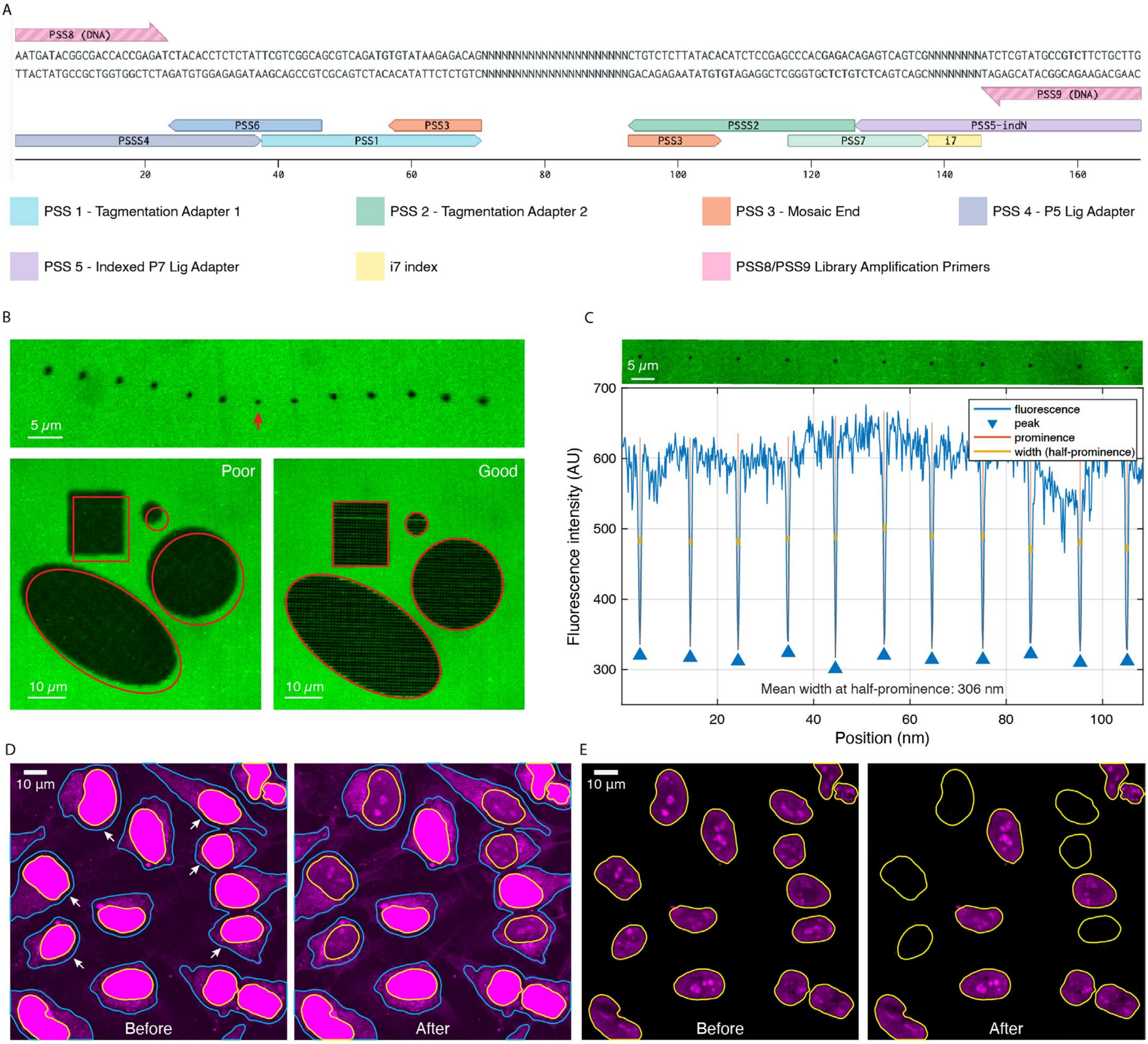

Extended Data Fig. 1 | Detailed Library structure and targeted illumination calibration. a) Detailed PSS library structure. Central N bases represent the genomic DNA fragment. **b**) Calibrating the focus and registration of the targeted illumination system. Top image strip shows the photocleaved area resulting from a single stimulation point as the focal plane of the targeted illumination device is varied. Red arrow indicates correct focus. Lower left image shows poor focus and poor registration (fuzzy edges and shift) while the lower right image shows proper calibration. **c**) Measuring the resolution of the targeted illumination. Image strip shows individual stimulation points on a photocleavable lawn of fluorescence. The fluorescence intensity (blue line) was measured by taking the minimum pixel value of the columns in the image strip above. The minimal spot size is taken as the full width at half-prominence (yellow bars). **d**) Images show cells before and after the uncaging process (target cells indicated with white arrows). Magenta color represents the fluorescence intensity of the fragment library (Alexa 546). The area between the blue and yellow outlines was used to calculate median-background-pixel intensity for each image. Image contrast was chosen to highlight cellular background fluorescence. **e**) Images showing background subtracted images of cells before and after the uncaging process. Magenta color represents the fluorescence intensity of the fragment library (Alexa 546). Yellow outlines indicate nuclear regions.

https://doi.org/10.1038/s41592-023-01845-8

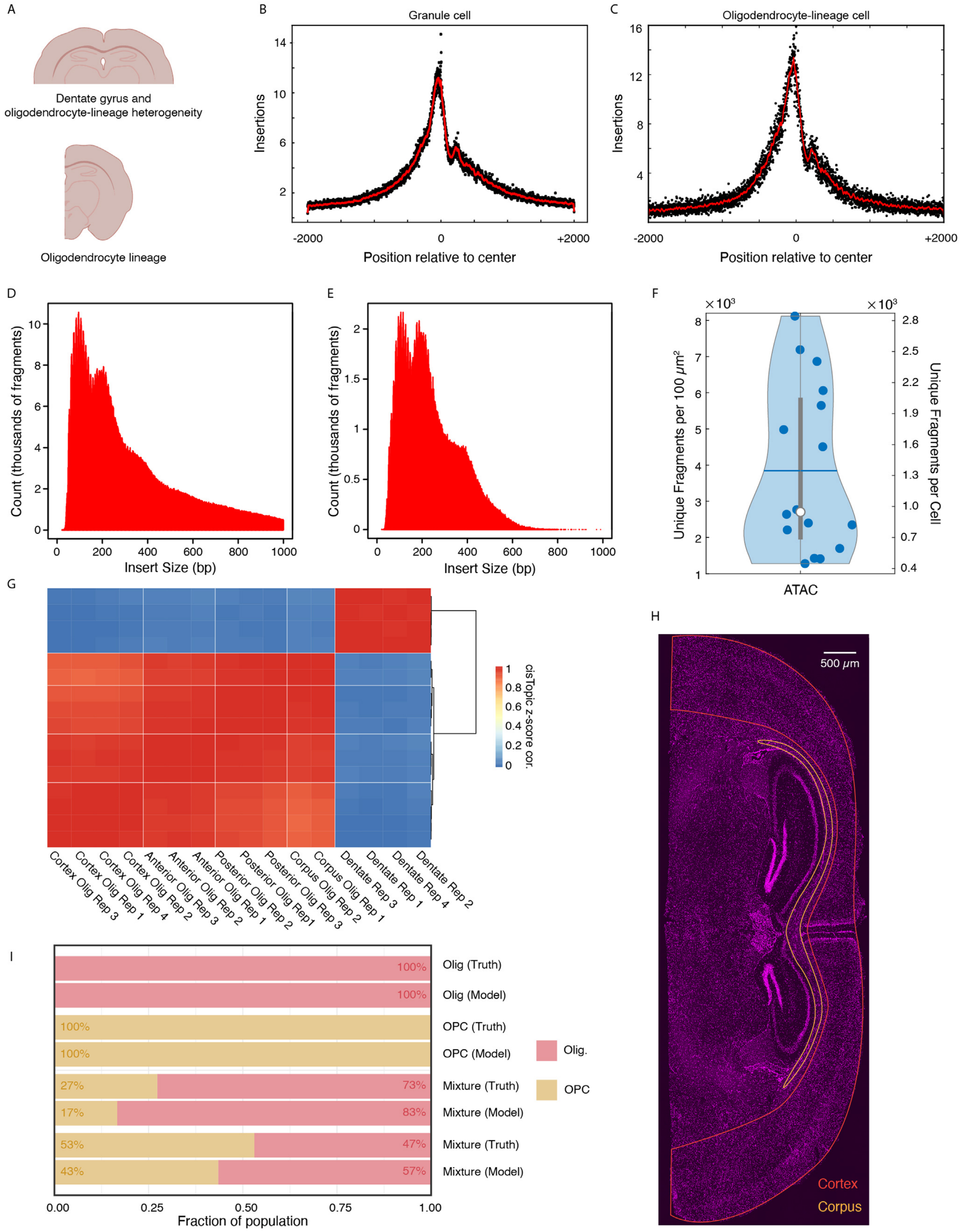

Extended Data Fig. 2 | See next page for caption.

Extended Data Fig. 2 | PSS in the mouse brain. a) Schematic illustrates tissue-section trimming for mouse-brain experiments. **b**) Typical TSS enrichment plot for dentate gyrus granular cells (single section). **c**) Typical TSS enrichment plot for oligodendrocyte lineage cells (single section). **d**) Typical insert size distribution for dentate gyrus granule cells. **e**) Typical inserts size distribution for oligodendrocyte-lineage cells. **f**) Violin plot showing the number of unique fragments detected per selected cell or selected 100 µm^2 area for all PSS ATAC-seq libraries from mouse brain samples (N = 16 tissue sections, 4 experiments). The blue line and white dot indicate the mean and median, respectively. The ends of the gray box represent the 25th and 75th percentiles, and the vertical gray line extends to the minimum and maximum data points. The violin shaped area represents the kernel density estimate of the raw data (blue dots). **g**) Pairwise correlation matrix (of cisTopic z-score) for individual replicates of all PSS ATAC-seq libraries (N = 16 tissue sections, 4 experiments). **h**) Low magnification scan of mouse hippocampal region with cortex (red) and corpus callosum (orange) regions outlined. Magenta color represents the fluorescence intensity from DRAQ5 DNA stain. **i**) Bar graph showing validation of decomposition algorithm using test oligodendrocyte and OPC data from an orthogonal single cell data. Truth bars represent the proportions in which the oligodendrocyte and OPC profiles were mixed. Model bars reflect the resulting fractional populations calculated by the decomposition algorithm (4 computational trials).

https://doi.org/10.1038/s41592-023-01845-8

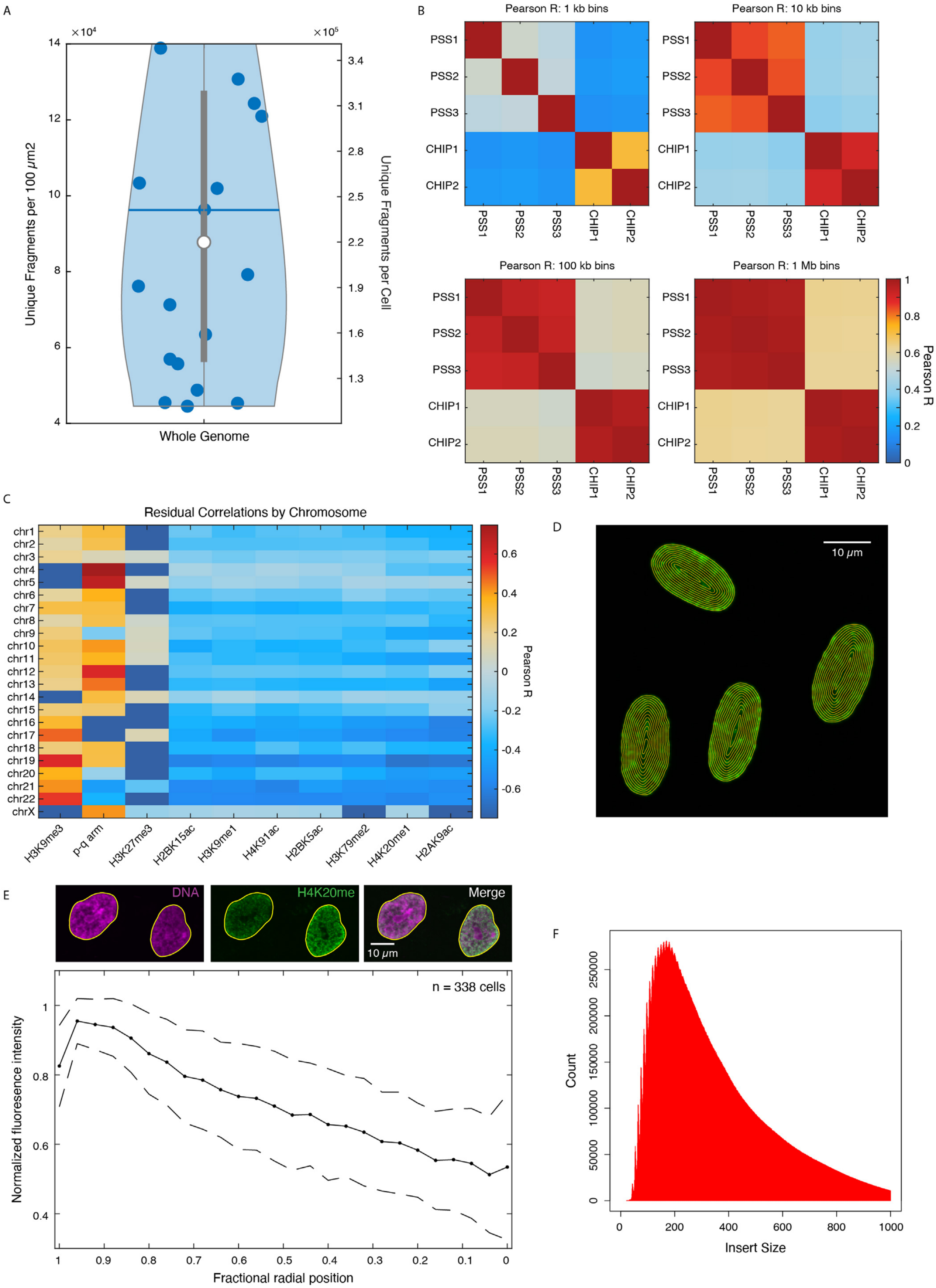

Extended Data Fig. 3 | See next page for caption.

Extended Data Fig. 3 | PSS at the nuclear periphery. a) Violin plot showing the number of unique fragments detected per selected cell or selected 100 μm^2 area for all PSS whole genome libraries (Fig. 1f and Fig. 3; N = 17 biological replicates across 2 experiments). The blue line and white dot indicate the mean and median, respectively. The ends of the gray box represent the 25th and 75th percentiles, and the vertical gray line extends to the minimum and maximum data points. The violin shaped area represents the kernel density estimate of the raw data (blue dots). **b**) Heatmaps showing pairwise Pearson correlation coefficients for PSS and lamin B1 ChIP-seq profiles at various bin sizes. **c**) Correlation between PSS nuclear periphery residuals (lamin B1 ChIP-seq signal removed) and histone ChIP-seq profiles from the ENCODE database. Dark blue boxes indicate a non-significant correlation. **d**) Images showing ring-like regions for calculating radial intensity profiles of histone modifications. **e**) Example images and radial intensity profile for H4K20me, a histone mark with a binding profile that is anticorrelated with the PSS nuclear periphery profile. **f**) Unimodal size distribution of sequenced fragments localized to the nuclear periphery indicates a loss of sensitivity to histone positioning.

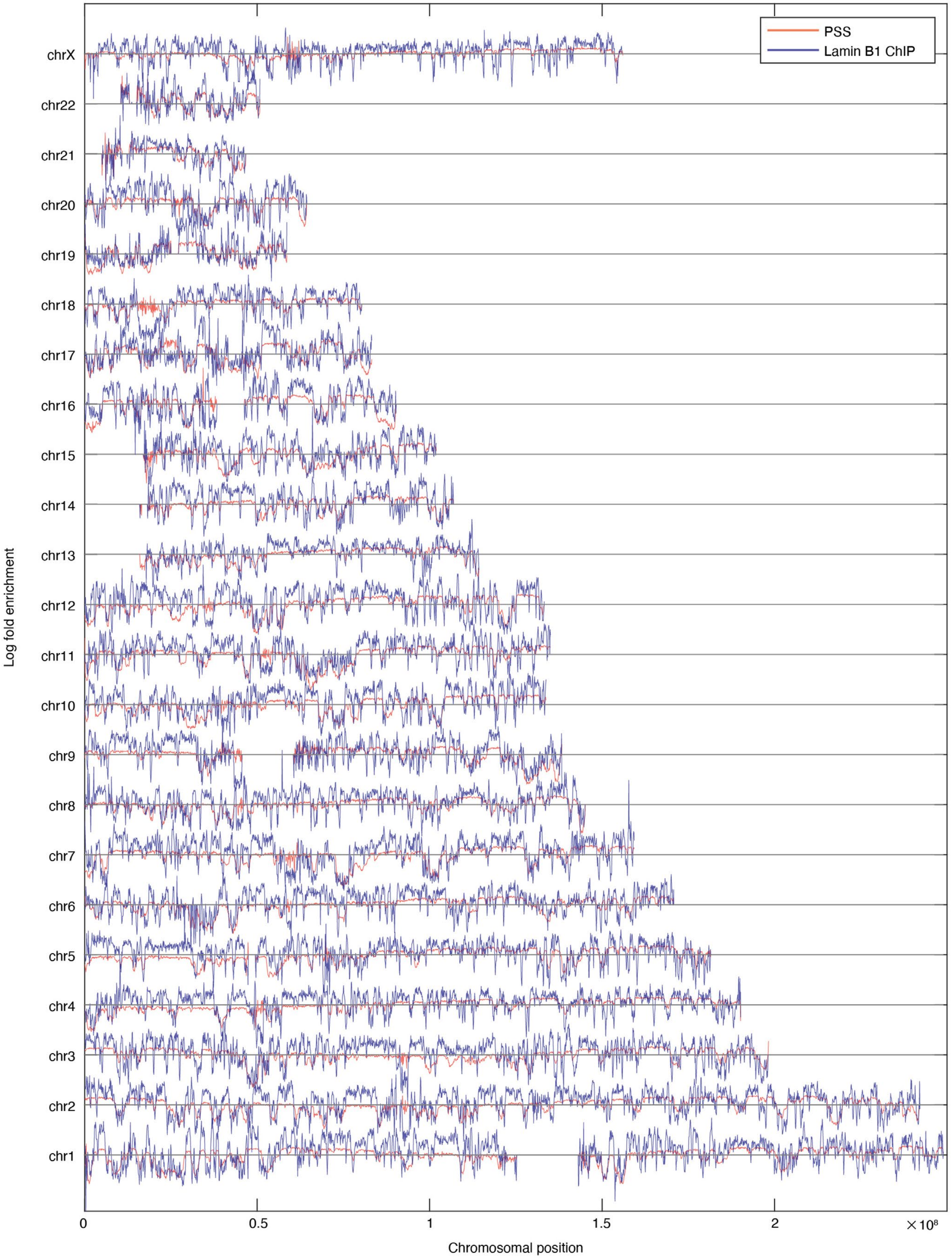

Extended Data Fig. 4 | PSS and Lamin B1 ChIP-seq enrichment across all chromosomes. Orange and blue lines show PSS and ChIP-seq log2 enrichment profiles, respectively. PSS enrichment profiles are aggregated across N = 3 replicates from 2 experiments.

Extended Data Table 1 | Oligonucleotide sequence list

Name	Sequence	Description
PSS1	/5Alex546N//iSpPC/TCGTCGGCAGCGTCAGATGTGTATAAGAGACAG	Photocleavable read 1 adapter
PSS2	/5Alex546N//iSpPC/GTCTCGTGGGCTCGGAGATGTGTATAAGAGACAG	Photocleavable read 2 adapter
PSS3	/5phos/C*T*G*T*C*T*C*T*T*A*T*A*C*A*/3ddC/	Blocked mosaic end
PSS4	AATGATACGGCGACCACCGAGATCTACACCTCTCTAT	P5 ligation adapter
PSS5-indN	CAAGCAGAAGACGGCATACGAGATBBBBBBBBCGACTGACTCT	Indexed P7 ligation adapter
PSS6	TGCCGACGAATAGAGAGGTGTAG/3ddC/	3’ blocked splint (P5 side)
PSS7	CCCACGAGACAGAGTCAGTCG/3ddC/	3’ blocked splint (P7 side)
PSS8	AATGATACGGCGACCACCGAGAT	Library amplification primer (P5 side)
PSS9	CAAGCAGAAGACGGCATACGAGAT	Library amplification primer (P7 side)

All oligonucleotides are written 5′ to 3′ using Integrated DNA Technologies modification codes. The B bases in the PSS5-indN primer represent a known barcode sequence for sample demultiplexing. For convenience, our complete set of indexed P7 ligation adapters is provided in Supplementary Table 2.

Extended Data Table 2 | Antibody List

Description	Catalog number
Rabbit monoclonal to Olig2	Abcam ab109186
Rabbit polyclonal to Lamin B1	Abcam ab16048
Rabbit polyclonal to Histone H3 (tri methyl K9)	Abcam ab8898
Rabbit monoclonal to Histone H4 (acetyl K8)	Abcam ab45166
Rabbit polyclonal to Histone H4 (mono methyl K20)	Abcam ab9051
Goat anti-Rabbit IgG (H+L) Highly Cross-Adsorbed Secondary Antibody, Alexa Fluor™ Plus 488	Invitrogen A32731

Table lists antibodies used in this study alongside the manufacturer and catalog number.

nature research

Corresponding author(s): Fei Chen
Jason Buenrostro

Last updated by author(s): Jun 14, 2022

Reporting Summary

Nature Research wishes to improve the reproducibility of the work that we publish. This form provides structure for consistency and transparency in reporting. For further information on Nature Research policies, see our Editorial Policies and the Editorial Policy Checklist.

Statistics

For all statistical analyses, confirm that the following items are present in the figure legend, table legend, main text, or Methods section.

n/a	Confirmed	
☐	☒	The exact sample size (*n*) for each experimental group/condition, given as a discrete number and unit of measurement
☐	☒	A statement on whether measurements were taken from distinct samples or whether the same sample was measured repeatedly
☐	☒	The statistical test(s) used AND whether they are one- or two-sided *Only common tests should be described solely by name; describe more complex techniques in the Methods section.*
☐	☒	A description of all covariates tested
☐	☒	A description of any assumptions or corrections, such as tests of normality and adjustment for multiple comparisons
☐	☒	A full description of the statistical parameters including central tendency (e.g. means) or other basic estimates (e.g. regression coefficient) AND variation (e.g. standard deviation) or associated estimates of uncertainty (e.g. confidence intervals)
☐	☒	For null hypothesis testing, the test statistic (e.g. *F*, *t*, *r*) with confidence intervals, effect sizes, degrees of freedom and *P* value noted *Give P values as exact values whenever suitable.*
☐	☒	For Bayesian analysis, information on the choice of priors and Markov chain Monte Carlo settings
☐	☒	For hierarchical and complex designs, identification of the appropriate level for tests and full reporting of outcomes
☐	☒	Estimates of effect sizes (e.g. Cohen's *d*, Pearson's *r*), indicating how they were calculated

Our web collection on statistics for biologists contains articles on many of the points above.

Software and code

Policy information about availability of computer code

Data collection	Nikon Elements AR
Data analysis	Sequencing alignment and pre-processing was performed using Bowtie2 version 1.2.2, Samtools version 1.9, bedtools version 2.29.2, and Picard version 2.20.7 (https://broadinstitute.github.io/picard/). Sequencing data were analyzed using cisTopic v3 (https://github.com/aertslab/cistopic) and chromVAR version 1.20.2 (https://github.com/GreenleafLab/chromVAR). Figure generation was scripted in Matlab R2022a, R3.5 and Python 2.7. PSS analysis scripts are available at https://github.com/sarahmangiameli/pss-tools.

For manuscripts utilizing custom algorithms or software that are central to the research but not yet described in published literature, software must be made available to editors and reviewers. We strongly encourage code deposition in a community repository (e.g. GitHub). See the Nature Research guidelines for submitting code & software for further information.

Data

Policy information about availability of data

All manuscripts must include a data availability statement. This statement should provide the following information, where applicable:

- Accession codes, unique identifiers, or web links for publicly available datasets
- A list of figures that have associated raw data
- A description of any restrictions on data availability

All raw PSS sequencing data are available from the Sequence Read archive under accession PRJNA938491 (cultured cell samples) and PRJNA938180 (mouse brain samples). Raw images corresponding to quantitative analyses in this study are available via Zenodo under the following DOIs: 10.5281/zenodo.7677794 (intensity decrease measurement), 10.5281/zenodo.7677827 (H3K9me3 radial intensity), 10.5281/zenodo.7677835 (H4K8ac radial intensity), 10.5281/zenodo.7677868 (H4K20me radial intensity). Single-cell ATAC-seq data (mouse hippocampus) from Sinnamon et al.23 are available through Gene Expression Omnibus (GEO; https://www.ncbi.nlm.nih.gov/geo/) under the accession GSE118987. Single-cell ATAC-seq data (whole mouse brain) from Lareau et al.24 were acquired via the GEO under accession number GSE123581. Histone ChIP-seq data were obtained from the ENCODE encyclopedia (https://www.encodeproject.org/) under the following accession numbers: ENCFF411NQX (H3K4ac), ENCFF039LQB and ENCFF966TQK (H4K8ac), ENCFF319QES (H2AK5ac), ENCFF048DVC (H4K91ac), ENCFF088QGG (H4K20me1), ENCFF083IVC and ENCFF640TNT (H3K79me1), ENCFF179YRO (H3K9me3), ENCFF704DVN (H3K27me3), ENCFF513JSZ (H2BK15ac), ENCFF672BWZ (H3K9me1), ENCFF048DVC (H4K91ac), ENCFF091RNK (H2BK5ac), ENCFF992CZO (H3K79me2), ENCFF058SOP (H2AK9ac). The H4K16ac data56 are available under GEO accession number GSE56307. Lamin B1 ChIP-seq data from Dou et al.37 are available under GEO accession number GSE63440.

Field-specific reporting

Please select the one below that is the best fit for your research. If you are not sure, read the appropriate sections before making your selection.

☒ Life sciences ☐ Behavioural & social sciences ☐ Ecological, evolutionary & environmental sciences

For a reference copy of the document with all sections, see nature.com/documents/nr-reporting-summary-flat.pdf

Life sciences study design

All studies must disclose on these points even when the disclosure is negative.

Sample size	No sample size calculation was performed. Each sample served as a proof-of-concept for the new technology, and biological replicates were performed to assess technical reproducibility.
Data exclusions	No data were excluded from analysis
Replication	All PSS experiments were preformed at least twice with consistent results. Imaging-only data (uncaging efficiency and radial intensity profiles) were derived from a single experiment.
Randomization	Brain sections an wells of cells were randomly paired with experimental conditions.
Blinding	Blinding is not relevant since this study is mainly a technical demonstration. Furthermore blinding was not possible since the data were largely collected and analyzed by the same individual.

Reporting for specific materials, systems and methods

We require information from authors about some types of materials, experimental systems and methods used in many studies. Here, indicate whether each material, system or method listed is relevant to your study. If you are not sure if a list item applies to your research, read the appropriate section before selecting a response.

Materials & experimental systems

n/a	Involved in the study	
☐	☒	Antibodies
☐	☒	Eukaryotic cell lines
☒	☐	Palaeontology and archaeology
☐	☒	Animals and other organisms
☒	☐	Human research participants
☒	☐	Clinical data
☒	☐	Dual use research of concern

Methods

n/a	Involved in the study	
☒	☐	ChIP-seq
☒	☐	Flow cytometry
☒	☐	MRI-based neuroimaging

Antibodies

Antibodies used	Rabbit monoclonal to Olig2 (Abcam ab109186); Rabbit polyclonal to Lamin B1 (Abcam ab16048); Rabbit polyclonal to Histone H3 (tri methyl K9) (Abcam ab8898); Goat anti-Rabbit IgG (H+L) Highly Cross-Adsorbed Secondary Antibody, Alexa Fluor™ Plus 488 (Invitrogen A32731), Rabbit monoclonal to Histone H4 (acetyl K8) (Abcam ab45166), Rabbit polyclonal to Histone H4 (mono methyl K20) (Abcam ab9051).
Validation	All antibodies in this study were obtained commercially, and validated by ensuring that the cellular localization was consistent with the images provided by the manufacturer.

Eukaryotic cell lines

Policy information about cell lines

Cell line source(s)	IMR90 (ATCC CCL-186), HeLa (ATCC CLL-2)

Authentication	Neither of the cell lines used were authenticated.
Mycoplasma contamination	Cell lines were tested for mycoplasma by the manufacturer prior to shipment.
Commonly misidentified lines (See ICLAC register)	N/A

Animals and other organisms

Policy information about studies involving animals; ARRIVE guidelines recommended for reporting animal research

Laboratory animals	We used wild-type adult C57BL/6 and CD1 mice in this study. Sex was not a relevant variable in our analysis but the randomly-selected mice were male.
Wild animals	This study did not involve wild animals.
Field-collected samples	This study did not involve samples collected from the field.
Ethics oversight	Animal procedures conducted at the Broad Institute complied with the US National Institute of Health Guide for the Care and Use of Laboratory Animals under protocol number 0211-06-18.

Note that full information on the approval of the study protocol must also be provided in the manuscript.